



HAL
open science

Basal stem cell progeny establish their apical surface in a junctional niche during turnover of an adult barrier epithelium

Anthony Galenza, Paola Moreno-Roman, Yu-Han Su, Lehi Acosta-Alvarez, Alain Debec, Antoine Guichet, Jon-Michael Knapp, Caroline Kizilyaprak, Bruno Humbel, Irina Kolotuev, et al.

► To cite this version:

Anthony Galenza, Paola Moreno-Roman, Yu-Han Su, Lehi Acosta-Alvarez, Alain Debec, et al.. Basal stem cell progeny establish their apical surface in a junctional niche during turnover of an adult barrier epithelium. *Nature Cell Biology*, 2023, 25 (5), pp.658-671. 10.1038/s41556-023-01116-w . hal-04290831

HAL Id: hal-04290831

<https://hal.science/hal-04290831v1>

Submitted on 17 Nov 2023

HAL is a multi-disciplinary open access archive for the deposit and dissemination of scientific research documents, whether they are published or not. The documents may come from teaching and research institutions in France or abroad, or from public or private research centers.

L'archive ouverte pluridisciplinaire **HAL**, est destinée au dépôt et à la diffusion de documents scientifiques de niveau recherche, publiés ou non, émanant des établissements d'enseignement et de recherche français ou étrangers, des laboratoires publics ou privés.

1
2
3
4
5
6 **Progenitor cell integration into a barrier epithelium during adult organ turnover**

7
8 Paola Moreno-Roman^{1,†}, Yu-Han Su¹, Anthony Galenza¹, Lehi Acosta-Alvarez¹,
9 Alain Debec^{2§}, Antoine Guichet², Jon-Michael Knapp³, Caroline Kizilyaprak⁴,
10 Bruno M. Humbel^{4,5,‡}, Irina Kolotuev⁴, & Lucy Erin O'Brien^{1*}
11
12
13
14
15
16
17
18
19
20
21
22
23

24 **Affiliations:**

25 ¹Department of Molecular & Cellular Physiology, Stanford School of Medicine, Stanford,
26 CA 94305 USA

27
28 ²Equipe Polarité et Morphogenèse, Institut Jacques Monod, CNRS-Université de Paris,
29 75205 Paris CEDEX 13 - France

30
31 ³Luminint Consulting Group, LLC.

32
33 ⁴Universite de Lausanne, Bâtiment Biophore, Quartier Sorge, CH-1015 Lausanne, Swit-
34 zerland

35
36 ⁵Department of Cell Biology and Neuroscience, Juntendo University Graduate School of
37 Medicine, Tokyo 113-8421, Japan

38
39
40 [†]Present address: Foldscope Instruments, Inc.

41
42 [‡]Present address: IMG, Okinawa Institute of Science and Technology, Tancha, Okinawa, Ja-
43 pan
44

45 §Present address: Institute of Ecology and Environmental Sciences, iEES, Sorbonne University,
46 UPEC, CNRS, IRD, INRA, F-75005 Paris, France

47

48

49 ***Corresponding author:** lucye@stanford.edu

50

51
52
53

54 **ABSTRACT**

55 Barrier epithelial organs face the constant challenge of sealing the interior body from the ex-
56 ternal environment while simultaneously replacing the cells that contact this environment. These
57 replacement cells – the progeny of basal stem cells – are born without apical, barrier-forming struc-
58 tures such as a protective, lumen-facing membrane and occluding junctions. How stem cell progeny
59 acquire these structures to become part of the barrier is unknown. Here we use Focused Ion Beam-
60 Scanning Electron Microscopy (FIB-SEM), Correlative Light-Electron Microscopy (CLEM), and vol-
61 umetric imaging of live and fixed organs to investigate progenitor integration in the intestinal epi-
62 thelium of adult *Drosophila*. We find that stem cell daughters gestate their future luminal-apical
63 membrane beneath a transient, basal niche formed by an umbrella-shaped occluding junction that
64 shelters the growing cell and adheres it to mature neighbor cells. The umbrella junction both targets
65 formation of a deep, microvilli-lined, apical invagination and closes it off from the contents of the
66 gut lumen. When the growing cell is sufficiently mature, the umbrella junction retracts to expose
67 this Pre-Assembled Apical Compartment (PAAC) to the gut lumen, thus incorporating the new cell
68 into the intestinal barrier. When we block umbrella junctions, stem cell daughters grow and attempt
69 to differentiate but fail to integrate; when we block cell growth, no umbrella junctions form and
70 daughters arrest in early differentiation. Thus, stem cell progeny build new barrier structures in the
71 shelter of a transient niche, where they are protected from luminal insults until they are prepared to
72 withstand them. By coordinating this dynamic junctional niche with progenitor cell differentiation, a
73 physiologically active epithelial organ incorporates new cells while upholding integrity of its barrier.

74
75

76 **INTRODUCTION**

77 Barrier epithelial organs protect the body interior from the external environment while per-
78 forming physiological processes that require direct exposure to this environment. For example, the
79 epithelium of the digestive tract both protects the body from gastric acid and enteric pathogens
80 while simultaneously breaking down and absorbing ingested nutrients. The dual roles of barrier
81 epithelia create a conundrum: Optimal physiological function requires that the tissue replace old,
82 spent cells with new stem cell progeny, but each individual progeny must be incorporated into the
83 epithelium without compromising barrier integrity (Guillot and Lecuit, 2013; Leblond, 1981; Liang et

84 al., 2017; Macara et al., 2014; Pellettieri and Alvarado, 2007). The cellular mechanisms which enable
85 stem cell progeny to seamlessly assimilate into a functioning barrier are poorly understood.

86 In all metazoans, epithelial barrier function arises from two conserved features of the epithe-
87 lial cells themselves. First, cell-cell occluding junctions – tight junctions in vertebrates, septate junc-
88 tions in invertebrates – create impermeable seals between cells (Varadarajan et al., 2019). Occluding
89 junctions encircle each epithelial cell at the lateral border of the apical membrane, creating a sealed
90 network that prevents even small molecules from freely passing between the lumen and the body
91 interior. Second, a lumen-facing, apical plasma membrane, tightly folded into microvilli or cilia,
92 forms a mucosal shield that resists corrosives, pathogens, and other luminal insults (Linden et al.,
93 2008; McGuckin et al., 2011; Overeem et al., 2015). This apical membrane is a hallmark of epithelial
94 differentiation and serves as the barrier’s direct interface with the outside world. In contrast, the
95 stem cells that renew many barrier epithelia lack occluding junctions and a lumen-contacting apical
96 membrane. Examples of such epithelia include the mammalian trachea (Evans and Moller, 1991;
97 Michael J. Evans, 2001; Rock et al., 2009; Sekiya et al., 1988), mammary gland (Chepko and Dickson,
98 2003; Chepko and Smith, 1997), prostate (Tsujiyama et al., 2002), cornea (Cotsarelis et al., 1989), and
99 olfactory lining (Leung et al., 2007), and the *Drosophila* adult midgut (Korzelius et al., 2014; Resnik-
100 Docampo et al., 2017; Xu et al., 2019). Stem cells in these tissues are much smaller than their mature
101 progeny; they inhabit the basal region of the epithelium, protected from luminal contents by the
102 mature cells’ occluding junction network.

103 Since stem cells lack barrier-forming structures, their progeny must generate these structures
104 *de novo* as they integrate into the barrier during terminal differentiation. Radial intercalation has
105 been proposed to be this integration mechanism (Walck-Shannon and Hardin, 2014; Sedzinski et al.,
106 2016; Chen et al., 2018). Many developing epithelial tissues use radial intercalation to merge basally
107 derived cells into an overlying epithelium (Merzdorf et al., 1998; Deblandre et al., 1999; Stubbs et al.,
108 2006; Voiculescu et al., 2007; McMahan et al., 2008; Campbell et al., 2010). In this process, a cell that
109 is born basal to the occluding junction network integrates into this network by moving apically
110 while wedging itself between pre-existing cells. When the tip of the intercalating cell reaches the epi-
111 thelium’s occluding junctions, the new cell forms occluding junctions with its neighbors. These SJs
112 begin as a pinpoint and morph into a ring that surrounds the cell’s nascent, lumen-facing apical
113 membrane. This apical membrane and its encircling occluding junction expand radially as the cell
114 grows to its final size (Stubbs et al., 2006; Sedzinski et al., 2016, 2017). Similar to these developmental
115 contexts, integration of adult stem cell progeny involves basal-to-apical movement and *de novo* for-

116 mation of barrier-forming structures. Whether stem cell progeny use radial intercalation or an alter-
117 nate, perhaps novel, mechanism, remains unexamined.

118 We leveraged recent advances in Focused Ion Beam-Scanning Electron Microscopy (FIB-
119 SEM), Correlative Light-Electron Microscopy (CLEM - (Burel et al., 2018)), and *in vivo* volumetric
120 confocal live imaging (Martin et al., 2018) to directly examine this question using the midgut of
121 adult *Drosophila*. Like many vertebrate barrier epithelia, the epithelial lining of the fly midgut is a
122 leakproof, pseudostratified epithelium that is continually renewed through the divisions of basal
123 stem cells (Lemaitre and Miguel-Aliaga, 2013). Investigating how new stem cell progeny assimilate
124 into this adult barrier epithelium, we found – unexpectedly – that assimilation occurs not by radial
125 intercalation but by a striking morphogenetic process that has not previously been described for any
126 tissue.

127 We discovered that as a stem cell daughter undergoes terminal differentiation, its nascent
128 occluding junctions form a transient, umbrella-shaped niche that supports development of the cell's
129 future, lumen-facing apical surface. This surface starts as an intercellular, localized delamination
130 within the umbrella-shaped junction. The delaminated membrane of the differentiating cell accumu-
131 lates apical markers, invaginates deeply into the cell's cytoplasm, and folds into microvilli in the
132 shelter of the junctional niche; these behaviors create a pre-assembled apical compartment (PAAC)
133 on the basal side of the epithelial barrier, protected from the contents of the gut lumen. In the final
134 phase of cell differentiation, the umbrella junction retracts to fuse the PAAC with the gut lumen,
135 and the apical membrane everts to form the mature cell's convex luminal surface.

136 The morphogenetic process of progenitor cell integration is coupled to growth that progeni-
137 tor cells undergo as they terminally differentiate. When we block stem cell daughters from integrat-
138 ing, they become trapped in a hybrid, partially differentiated state and accumulate on the basal side
139 of the epithelium. These animals die prematurely, implying that organismal longevity is compro-
140 mised when the intestinal barrier is not properly replenished.

141 We suggest that PAAC-mediated integration enables stem cell progeny to generate lumen-
142 facing cell surfaces in a space that is protected from luminal insults, thus enabling new cells to be
143 added seamlessly to a physiologically active barrier epithelium.

144 RESULTS

145 Mature intestinal enterocytes form the bulk of the *Drosophila* midgut and are responsible for
146 its barrier function. Like their vertebrate counterparts, *Drosophila* enterocytes are bonded together by
147 apical occluding junctions (Figs. 1A & 2A). In the fly gut, these occluding junctions are smooth sep-

148 tate junctions (SJs) (Furuse and Izumi, 2017). Also like their vertebrate counterparts, *Drosophila* en-
149 terocytes display an apical brush border composed of long, dense microvilli (Fig. 2A); the brush
150 border both absorbs nutrients and protects against luminal pathogens.

151 Enterocytes are terminally differentiated and post-mitotic. When shed through damage or
152 death, they are replaced by division of resident stem cells (Micchelli and Perrimon, 2006; Ohlstein
153 and Spradling, 2006; Jiang and Edgar, 2009; Liang et al., 2017). Stem cell progeny that are fated to
154 become enterocytes must first pass through an intermediate, post-mitotic stage called an enteroblast
155 (Ohlstein and Spradling, 2007; Bardin et al., 2010; Perdigo et al., 2011) (Figure 1A). Enteroblast
156 identity is determined by activation of the Notch receptor and can be visualized using Notch report-
157 ers such as *Su(H)-GFP::nls* and *Su(H)-lacZ* (Ohlstein and Spradling, 2007; Bardin et al., 2010; Perdigo-
158 to et al., 2011; de Navascués et al., 2012). As enteroblasts differentiate to enterocytes, they endorepli-
159 cate from 2N to 32-64N and increase in volume by ~30x (Xiang et al., 2017).

160 **Stem cell progeny initiate new SJs at discrete contact points with mature cells**

161 We were intrigued by prior observations that stem cells lack SJs (Korzelius et al., 2014; Res-
162 nik-Docampo et al., 2017; Xu et al., 2019) because this implies that differentiating cells must form SJs
163 *de novo* and integrate themselves into the enterocytes' leakproof SJ network. We sought to determine
164 when, where, and how *de novo* SJ formation occurs. First, we asked whether enteroblasts form SJs
165 with their mature enterocyte neighbors (Figs. 1 & 2). If so, then SJ components should localize to en-
166 teroblast-enterocyte interfaces. To investigate this prediction, we used midguts that expressed
167 markers to distinguish enteroblasts, enterocytes, and stem cells. We immunostained them for the SJ
168 components Snakeskin (Ssk) and Tetraspanin2A (Tsp2A) (Yanagihashi et al., 2012; Izumi et al., 2016),
169 then performed 5-channel multi-photon laser scanning microscopy to visualize SJs in the context of
170 identified cells.

171 We observed SJ components at nearly all enteroblast-enterocyte interfaces, but not at the vast
172 majority of stem cell-enterocyte interfaces nor at any stem cell-enteroblast interfaces. 89% of stem
173 cells (*escargot*GAL4, *UAS-his2b::CFP* (*esg*⁺), Armadillo (*Arm*⁺), *Su(H)-GFP::nls*⁻) exhibited no co-
174 localization with SJ components (n=119 stem cells from 5 guts) (Fig. 1B & 1E), as expected (Korzelius
175 et al., 2014; Resnik-Docampo et al., 2017; Xu et al., 2019). By contrast, 92% of enteroblasts (*esg*⁺, *Arm*⁺,
176 *Su(H)-GFP::nls*⁺) (Figs. 1C, 1D, 1F & 1G) overlapped with enterocyte-enterocyte SJs (n=125 entero-
177 blasts from 5 guts). Many SJ-contacting enteroblasts exhibited small, presumably diploid, nuclei,
178 which suggests that these contacts are formed in initial stages of enteroblast fate determination.

179 Enteroblast SJ staining invariably localized to the apical-most tips (apex) of the enteroblasts,
180 where it overlapped with the basal terminus of the enterocyte SJs. This overlap might represent ei-
181 ther *bona fide* adhesion septa between enteroblasts and enterocytes or else the mere physical proxim-
182 ity without formation of true adhesion septa. To distinguish these scenarios, we performed correla-
183 tive light-electron microscopy (CLEM) (Kolotuev, 2014) on *Su(H)-GFP::nls*-expressing midguts to
184 identify the GFP-labelled enteroblasts. FIB was performed in random positions of the midgut R4c
185 region; GFP-labeled enteroblasts were identified; and interfaces between these enteroblasts and
186 neighbor enterocytes were examined for potential SJ septa.

187 In EM, SJ septa characteristically appear as electron-dense structures that ‘fuse’ together the
188 apposing plasma membranes of adjacent cells. As expected, enterocyte-enterocyte septa fused to-
189 gether the apical-most regions of the cells’ lateral membranes, directly adjacent to their microvilli-
190 rich brush borders (Fig. 2A). However, when enterocytes were next to an enteroblast (Figs. 2B-2E),
191 their SJs extended basally toward the enteroblast (red pseudocolor in Fig. 2B’’) and fused with en-
192 teroblast plasma membrane at its apex (arrowheads). These observations demonstrate that entero-
193 blasts form *bona fide* SJ septa with mature neighbor cells. In addition, they imply that light-
194 microscopy visualized overlap of immunostained SJ components with enteroblast cell membranes
195 (Fig. 1) are sites of new SJ formation.

196 To understand the three-dimensional structure of enteroblast-enterocyte SJs, we performed
197 array tomography. We transformed the tomograms into volumetric renderings of individual cells
198 and their SJ interfaces. Fig. 2C and Video 1 show the volumetric rendering of a 30-slice series sur-
199 rounding the CLEM image in Fig. 2B. The apex of this diploid (presumably, newly determined) en-
200 teroblast (red) exhibits three finger-like projections (arrowheads), each of which forms a point-like,
201 discrete SJ (green) with one of its three neighbor enterocytes (blue; labelled 1-3 in Fig. 2B). No SJs are
202 visible between the enteroblast and an adjacent, *Su(H)-GFP::nls*-negative stem cell (yellow). The en-
203 teroblast’s three point-like SJs contact the three enterocyte SJs (pink, pale blue, and purple) at the
204 latter’s basal rim. Importantly, we found no discontinuities between the new, enteroblast-enterocyte
205 SJs (overlap between green and either pink, pale blue, or purple) and the pre-existing, enterocyte-
206 enterocyte SJs (overlap between pink and pale blue, pink and purple, or pale blue and purple). This
207 structural continuity suggests that the pre-existing, enterocyte-enterocyte SJ guides the localization
208 of initial SJ contacts between enterocytes and the new enteroblast.

209 **SJ contacts develop into a large, umbrella-shaped SJ that covers the enteroblast apex and**
210 **extends toward the basal epithelium**

211 We next generated a volumetric rendering of a larger (hence, likely older) enteroblast (red)
212 from a 413-slice FIB-SEM tomographic series that spanned a 35.6 μm x 35.6 μm x 4.5 μm tissue volume.
213 A single slice from this series is shown in Figs. 2D-D' and Fig. S1, and the volumetric rendering is
214 shown in Figure 2E and Video 2. In contrast to the nascent SJ contacts formed by a young entero-
215 blast (Figures 2B & 2C), the SJ (green) of this older enteroblast is an expansive, adhesive 'zone'
216 whose shape resembles an umbrella. This umbrella SJ fuses the pyramidal enteroblast to three ma-
217 ture neighbor cells: the SJs (pink and purple) of two enterocytes (blue; labelled 1 and 2 in Figs. 2D &
218 2E) and those of an enteroendocrine cell (pale blue; labelled 3 in Fig. 2D). No SJs are visible at the
219 interface between the enteroblast and a presumptive stem cell (yellow). As with SJs of the young en-
220 teroblast (Fig. 2B-C), the SJs between the older enteroblast and its neighbor enterocytes (green/pink
221 overlap and green/purple overlap) are continuous with the SJ that had previously formed between
222 the enterocytes themselves (pink/purple overlap).

223 Importantly, the umbrella SJ extends unusually far toward the basal epithelium – a feature
224 that is incompatible with a simple model of radial intercalation. SJs typically occupy a narrow band
225 at the apical border of the enterocytes' lateral membranes (Fig. 2A; also in Fig. 2E and E', the purple
226 SJ on left side of enterocyte 1 and pink SJ on right side of enterocyte 2). In radial intercalation, the SJ
227 initiates at the point where the new cell's apical tip becomes co-planar with the organ's mature SJ
228 network; hence, the new SJ grows to a narrow width that matches that of mature SJs (Walck-
229 Shannon and Hardin, 2014; Stubbs et al., 2006; Sedzinski et al., 2016, 2017; Chen et al., 2018). Howev-
230 er, an enteroblast's umbrella SJ spreads basally along two-thirds of the enterocytes' lateral mem-
231 branes and shrouds the top third of the enteroblast (Fig. 2E, green SJ and associated pink and purple
232 SJs; Video 2). This basally-extended umbrella shape implies an alternate mode of integration in
233 which the new SJ forms basal to the organ's mature SJ network.

234 **Cloning Meduse, an actin-associated protein that localizes to the brush border of midgut**
235 **enterocytes**

236 The second component of the gut's barrier structure is collectively formed by the apical cell
237 surfaces that line the gut lumen. Mature enterocytes fold these surfaces into long, dense microvilli,
238 forming the intestinal brush border (Fig. 2A). Mature enterocytes also exhibit apical-basal polarity,
239 as characterized by lumen-polarized localization of cytoskeleton-associated proteins such as Moesin,
240 Karst (β_{H} -spectrin), and Myosin7a (Baumann, 2001; Chen et al., 2018).

241 Another luminally polarized marker is provided by the splice-trap transposon line
242 A142(Bobinnec et al., 2003; Buchon et al., 2013), which expresses a GFP fusion protein that co-
243 localizes with Moesin at or near enterocyte microvilli (Fig. 3A-C). We found that this transposon is
244 inserted into CG2556 (Fig. S2A), a previously uncharacterized gene that does not appear to have ver-
245 tebrate homologs. Since the filamentous appearance of the A142 fusion protein in egg chambers is
246 reminiscent of sea jelly tentacles (Fig. S2B), we named this gene Meduse (Mdu). Mdu is predicted to
247 be a 470 amino-acid, 51 kDa protein whose sole identifiable motif is an actin binding domain. This
248 putative actin-binding function is consistent with localization of the A142 splice trap to the apical
249 brush border of enterocytes and with actin filaments in Stage 10 egg chambers, the latter of which is
250 latrunculin-sensitive (Fig. S2B-C).

251 **The umbrella SJ is a transient niche for formation of the new cell's future lumenal-apical** 252 **surface**

253 During development of tubular epithelial organs, cells generally couple the formation of a
254 lumen-contacting cell surface to the formation of apical features including microvilli, occluding junc-
255 tions, and apically polarized membrane and cytoskeletal proteins (Blasky et al., 2015; Datta et al.,
256 2011; O'Brien et al., 2002; Sigurbjörnsdóttir et al., 2014). By comparison, stem cells in the adult fly gut
257 lack this entire suite of lumenal-apical features (Figs. 2B-2E) (Chen et al., 2018). How do stem cell
258 progeny generate a lumenal-apical surface as they differentiate, and how do they coordinate apical
259 morphogenesis with SJ formation and epithelial integration?

260 To address this question, we used high-resolution images of fixed guts to identify cells at dis-
261 tinct stages of differentiation, assessed the localization of apical markers, and correlated apical
262 marker localization to SJ maturation (Figs. 3 & S2 and Video 3). Midguts that express Su(H)-lacZ
263 were used because the long perdurance of β -galactosidase (>20 h half-life (Bachmair et al., 1986))
264 makes it possible to identify early-stage enterocytes that have recently turned off enteroblast-specific
265 *Su(H)* activity but have not yet completed terminal morphogenesis (Fig. S3). Comparing apical
266 marker localization, SJ morphology, and the cytoplasmic and nuclear sizes of Su(H)-lacZ⁺ cells, we
267 distinguished four stages of apical membrane morphogenesis.

268 In Stage 1 (left-most column in Fig. 3), enteroblasts are small, and their nuclei appear diploid;
269 this stem-like appearance is consistent with the cells being in early stages of terminal differentiation.
270 Stage 1 enteroblasts lack apical polarity, but they have formed SJ contacts with enterocytes. The few
271 apical markers that are expressed, such as Moesin (Figs. 3A and C), do not show a polarized distri-
272 bution; other apical markers, such as Karst and Mdu (Figs. 3B and 3C), are not detectable. The apex
273 of Stage 1 enteroblasts contacts the basal terminus of enterocyte-enterocyte SJs, as revealed by locali-

274 zation of SJ components Tsp2A and Ssk (Figs. 3A and 3C). We interpret these SJ contacts to be nas-
275 cent, point-like SJs, similar to those formed by the enteroblast in Figs. 2B and 2C.

276 In Stage 2 (Fig 3, second column from left), enteroblasts preferentially localize apical markers
277 to their apex; this enrichment forms a bright plaque that is covered by broadened SJ contacts (Figs.
278 3A-C). We suggest that this apical plaque represents early stages of polarization since low levels of
279 apical markers persist at other cortical regions. The enteroblast SJ grows to cover the cell's entire
280 apex; we infer that these Stage 2 SJs are similar to the SJ in Figs. 2D and 2E. With respect to mor-
281 phology, some Stage 2 enteroblasts (e.g. Figs. 3B and 3C) are similar in cytoplasmic and nuclear size
282 to Stage 1 enteroblasts; other Stage 2 enteroblasts are slightly larger, and their nuclei appear inter-
283 mediate in ploidy between 2N stem cells and 32-64N, mature enterocytes (e.g. Fig. 3A).

284 In Stage 3 (Fig. 3, third column from left), the differentiating cells resemble immature entero-
285 cytes. Their cytoplasmic and nuclear volumes are larger than Stage 1-2 enteroblasts, yet smaller than
286 mature enterocytes, and their low levels of β -galactosidase suggest that Su(H) enhancer activity was
287 diminishing. We refer to these cells as pre-enterocytes. Apical markers – now highly expressed –
288 localize to a conspicuous, concave structure that is covered by the broad, umbrella-shaped SJ sheet
289 that we described above. These concave structures are the morphological hallmarks of Stage 3. With
290 diameters up to 12 μm – roughly the diameter of a mature enterocyte – they often fill the apex of the
291 pre-enterocytes. We were surprised to discover that they are topologically discontinuous with the
292 midgut lumen (Video 3), another feature that is incompatible with radial intercalation. Instead, we
293 conjecture that these structures are precursors of the pre-enterocytes' future lumen-contacting sur-
294 face. Hence, we designate them as Pre-Assembled Apical Compartments (PAACs).

295 In Stage 4, (Fig. 3, right column), pre-enterocytes finish integrating into the gut epithelium by
296 acquiring a topology of cell-cell interfaces that is equivalent to mature enterocytes. Stage 4 cells are
297 circumscribed (rather than covered as in previous stages) by SJs, and they now possess a lumen-
298 contacting apical surface. The shapes of Stage 4 lumen-contacting surfaces and Stage 3 PAACs are
299 highly similar, which suggests that the PAAC opens up to the gut lumen via remodeling of its over-
300 lying umbrella SJ into a ring. Stage 4 cells are smaller in cytoplasmic volume and nuclear size com-
301 pared to mature enterocytes. In a final Stage 5 (Fig. S3D), the cell acquires its mature size and ploidy
302 and everts its luminal-apical surface to form a convex shape, thus completing terminal differentia-
303 tion.

304 Altogether, this morphogenetic sequence reveals that midgut stem cell progeny do not form
305 new SJs and an apical membrane via radial intercalation into the epithelial barrier. Rather, they form
306 these barrier structures while still in the basal epithelium, protected by the mature barrier.

307 **Live imaging of enteroblast-enterocyte integration**

308 We next asked whether live imaging corroborates the four-stage sequence (Fig. S3D) of en-
309 teroblast-enterocyte integration implied by fixed samples. To address this question, We performed
310 continuous time-lapse imaging using Windowmount methodology, in which volumetric movies of
311 physiologically functioning guts are captured in live animals through a window cut into the dorsal
312 cuticle (Fig. 4A) (Martin et al., 2018). Prior analyses of stem cell clones in both fixed guts (He et al.,
313 2019; de Navascués et al., 2012) and intravital live imaging (Koyama et al., 2020) suggest that most
314 enteroblasts require >24 h to differentiate into enterocytes. Although this time frame is longer than
315 the 16-20 h viability of animals during Windowmount (Martin et al., 2018), longitudinal imaging
316 suggests that some cells differentiate in <24 h (Koyama et al., 2020). Therefore, we aspired to capture
317 these faster cells.

318 We first examined live dynamics of SJs. From nine movies of *GS5966>tsp2A::GFP; Su(H)-*
319 *mCherry* midguts with durations from 7.25-20 h, we identified one movie in which an mCherry-
320 expressing cell increased in cross-sectional area by nearly three-fold (Fig. 4B & 4D, and Video 4); this
321 dramatic growth is an identifying feature of enteroblast-enterocyte differentiation. To determine
322 whether the Tsp2A::GFP-labelled SJ associated with this cell exhibited dynamics consistent with the
323 mechanism implied by Fig. 3, we analyzed an orthogonal view through the cell's apical-basal axis
324 (Fig. 4C). In the movie's initial 105 min, the SJ that contacted the differentiating cell grew broader
325 and ultimately covered the cell's entire apex (Fig. 4C, arrow in 0- and 90-min panels; Video 4, 0-105
326 min). This broadening is consistent with the notion that SJs expand from discrete contact points in
327 Stage 1 (Fig. 2C, Fig. 3A & 3B, and Video 1) to an umbrella shape in Stages 2 and 3 (Fig. 2E, Video 2,
328 Fig. 3A & B, Fig. 5D, and Video 6). Between 120-285 min, a hollow space developed along the SJ's
329 apical-basal axis; simultaneously, the SJ extended along the lateral faces of the now-larger cell (Fig.
330 4C, arrows (SJ) and asterisks (hollowing) in 195- and 285-min panels; Video 4, 120-285 min). This
331 hollowing and lateral extension are consistent with remodeling of the SJ from an overlying sheet in
332 Stage 3 to a circumscribing ring in Stage 4 (Fig. 3A & 3B). Overall, these live SJ dynamics support the
333 morphogenetic sequence suggested by the fixed analyses in Fig. 3.

334 We next examined live dynamics of the apical membrane using midguts that expressed the
335 apical marker Moesin::GFP and the nuclear marker His2av::mRFP (Fig. 4E and Video 5). The
336 Moesin::GFP-labelled luminal-apical membranes appeared as a convoluted surface atop the gut
337 cells' nuclei because the apical surface of mature enterocyte is domed (e.g. Fig. 2A). Basal to the lu-
338 menal-apical membranes, we frequently observed GFP-labelled structures that were fainter in inten-
339 sity and concave in shape. We conjecture that these structures are PAACs. While most PAACs did

340 not dramatically change in shape or size during imaging, some PAACs became brighter and deeper
341 over time (*e.g.*, Fig. 4E and Video 5). This evolution is consistent with Stages 3-4 of differentiation,
342 during which PAACs initially form and subsequently become larger and more enriched for apical
343 markers (Fig. 3, Stages 2-3). Overall, we conclude that live imaging of SJ and apical membrane dy-
344 namics provides additional support for the four-stage mechanism suggested by fixed tissues.

345 **PAACs are intercellular lumens formed by asymmetric pre-enterocyte apical membranes** 346 **and enterocyte basolateral membranes**

347 Our finding that PAACs are physically distinct from the gut's lumenal-apical surface raises
348 basic questions about the nature of these structures: Are they intracellular or intercellular? What is
349 their relationship to the developing SJ? Does their apical polarity correspond to a mature brush bor-
350 der? To gain insight into these and other questions, we examined the PAACs' ultrastructure in FIB-
351 SEM tomographic series.

352 To identify putative PAACs, we first identified pre-enterocytes by looking for polyploid cells
353 that lacked a visible lumenal-apical surface. We noticed that the apexes of such pre-enterocytes fre-
354 quently contained membrane-bound, ellipsoid ultrastructures (Fig. 5A-cyan box, and Fig. 5B) whose
355 shape and cellular position resembled PAACs. These structures enclosed prominent lumens that are
356 distinct from the gut lumen, circumscribed by SJs, and lined with microvilli. The microvilli are
357 densely arrayed, similar to brush border microvilli, but they are shorter, which suggests they are
358 immature. Notably, Moesin, which outlines PAACs in confocal micrographs (Fig. 3 and Video 3), is
359 a marker of microvilli in other *Drosophila* epithelia (Edwards et al., 1997; Lattner et al., 2019). We
360 also found sausage-shaped (allantoid) ultrastructures that, like the ellipsoids, are lined with dense
361 microvilli and circumscribed by SJs (Fig. 5A-magenta box, and Fig. 5C). The allantoids' lumens are
362 extremely slender, suggesting that they may be newly formed. Given these features, we conjecture
363 that the ellipsoid ultrastructures are PAACs and the allantoid ultrastructures are their precursors.

364 We took advantage of our FIB-SEM series to investigate whether PAACs are intracellular
365 compartments that develop within a pre-enterocyte, akin to the large apical endosomes (vacuolar
366 apical compartments/apicosomes) observed in mammalian cells (Gilbert and Rodriguez-Boulan,
367 1991; Taniguchi et al., 2017; Vega-Salas, 1988) or intercellular compartments that develop between a
368 pre-enterocyte and its mature enterocyte neighbors. We selected series that captured the near-
369 complete volume of individual PAACs or PAAC precursors, and we analyzed their membrane to-
370 pologies slice-by-slice (Figs. 5B and 5C). We also generated a volumetric rendering of a 200-slice FIB-
371 SEM tomographic series that contained a PAAC, a PAAC precursor, and their associated pre-
372 enterocyte within a tissue volume of $40.2\ \mu\text{m} \times 23.9\ \mu\text{m} \times 8\ \mu\text{m}$ (Fig. 5D and Video 6).

373 These analyses invariably uncovered a region in which pre-enterocyte and mature enterocyte
374 membranes separate from each other to form the PAAC's luminal space (Fig. 5B and Video 6). Thus,
375 PAACs are intercellular. The PAAC lumen is surrounded by an expansive SJ that adheres the pre-
376 enterocyte to mature enterocytes; this SJ separates the PAAC from the gut's central lumen. The ul-
377 trastructure of the PAAC-associated SJ is consistent with the SJs we observed in immunostained,
378 Stage 3 pre-enterocytes (Fig. 3 and Video 3). PAAC precursors – even very small ones – also com-
379 prise an intercellular lumen surrounded by an expansive SJ. We did not observe any microvilli-lined
380 compartments that were entirely intracellular. The similar topology of PAACs and PAAC precursors
381 suggests that PAACs initiate via de-adhesion of apposing plasma membranes rather than fusion of
382 an intracellular compartment with the SJ.

383 **PAACs' split apical/basolateral polarity is unique for a lumen-encompassing structure**

384 PAAC-forming pre- and mature enterocytes make markedly unequal contributions to the
385 PAAC's overall morphology. The pre-enterocyte plasma membrane represents the vast majority of a
386 PAAC's total surface area. It folds inward at nearly 180 degrees (arrow in Fig. 5B) to create a deep
387 invagination into the pre-enterocyte cytoplasm. This invagination accounts for most of the PAAC's
388 luminal volume and evokes a scenario in which PAAC development is driven by inward folding of
389 the pre-enterocyte plasma membrane. In contrast to the structured folds of the pre-enterocyte mem-
390 brane, the mature enterocyte membranes are amorphous and rest like a blobby lid atop the PAAC
391 lumen (Fig. 5B). These differences are even more extreme in PAAC precursors (Fig. 5C).

392 The contrast between the structured pre-enterocyte membrane and the amorphous entero-
393 cyte membrane corresponds to a second – unprecedented – asymmetry of PAACs: their luminal po-
394 larity is split. The PAAC's pre-enterocyte membrane is apical while the partner enterocyte mem-
395 brane(s), which lacks apical markers (Video 3) and microvilli (Figs. 5B & 5C, and Video 6), is by de-
396 fault basolateral. To our knowledge, this combination has not previously been reported for any epi-
397 thelial lumen either in cell culture or *in vivo*. Rather, epithelial lumens to date have been either uni-
398 formly apical (Blasky et al., 2015; Datta et al., 2011; O'Brien et al., 2002), or, in some rare, experimen-
399 tally induced cases, uniformly basolateral (Lowery et al., 2009; Wang et al., 1990). However, these
400 prior studies examined lumens that form between cells at similar differentiation states; we conjec-
401 ture that the PAACs' unique asymmetries derive from their origin between cells at distinct differen-
402 tiation states.

403 **Enteroblasts must form SJs to integrate and mature into enterocytes**

404 Our data reveal that as stem cell daughters differentiate, they initiate epithelial integration
405 by forming new, sheet-like SJs with mature neighbor cells. What happens when SJ formation is
406 blocked? To examine this question, we generated "SJ-less" enteroblasts and assessed their ability to
407 integrate and differentiate. We inhibited expression of the SJ component *ssk* specifically in entero-
408 blasts by using the enteroblast driver *Su(H)-GAL4* to express a *UAS-sskRNAi* transgene under con-
409 trol of temperature-sensitive *GAL80^{ts}* (McGuire et al., 2003) (genotype henceforth referred to as
410 *Su(H)^{ts}>sskRNAi*). A *UAS-GFP* transgene was also included to identify the RNAi-expressing cells.
411 The *sskRNAi* hairpin was expressed from days 0-4 of adult life, after which midguts were harvested
412 and analyzed. To confirm that *sskRNAi* prevented SJ formation, we performed immunostaining for
413 another SJ component, Coracle. Whereas Coracle localized to the apex of *Su(H)^{ts}*-expressing control
414 cells, it localized to the cytoplasm of *Su(H)^{ts}>sskRNAi* cells (Figs. 6A & 6B). This redistribution im-
415 plies that *sskRNAi* expression prevents proper formation of SJs.

416 *Su(H)^{ts}>sskRNAi* cells categorically failed to integrate into the gut epithelium. Instead of
417 reaching the gut's central lumen, these cells accumulated beneath the gut's SJ network (Figs. 6A &
418 6B). Although this basal localization is typical of enteroblasts, *Su(H)^{ts}>sskRNAi* cells did not arrest in
419 an enteroblast state. Rather, they grew in volume and endoreplicated their nuclei (Fig. 6C and Figs.
420 S5A & S5B), two behaviors characteristic of pre-enterocytes (Fig. 3, Stages 3 & 4). Yet unlike pre-
421 enterocytes, *Su(H)^{ts}>sskRNAi* cells did not adopt a cuboidal or columnar shape and instead became
422 blob-shaped. Similar behaviors were exhibited by MARCM-generated stem cell clones (Lee and Luo,
423 1999) that were genetically null for SJ components *tsp2A* (Chen et al., 2018) and *mesh* (Fig. S5E & S5F).
424 Thus even as SJ-less cells achieve mature size, they do not become part of the epithelium.

425 The indeterminate morphology of *Su(H)^{ts}>sskRNAi* cells was accompanied by inappropriate,
426 mixed expression of fate-specific transcription factors. Whereas the stem cell/enteroblast transcrip-
427 tion factor Sox100B (Doupé et al., 2018; Jin et al., 2020; Meng et al., 2020) was expressed by both con-
428 trol *Su(H)* and *Su(H)^{ts}>sskRNAi* cells (Figs. S5A & S5B), the enterocyte transcription factor Pdm1
429 (Dantoft et al., 2013; Korzelius et al., 2014; Lee et al., 2009) was absent from control *Su(H)* cells yet
430 expressed in *Su(H)^{ts}>sskRNAi* cells (Figs. S5C & S5D). Similar, mixed patterns of marker expression
431 were observed by Xu and colleagues upon enteroblast-specific depletion of the SJ component *tsp2A*
432 (Xu et al., 2019).

433 Altogether, these findings imply that SJ-less cells become trapped in an abnormal, hybrid cel-
434 lular state in which the distinct features of enteroblasts and enterocytes co-exist abnormally.

435 **Cell growth is required for integration, independent of SJs**

436 Having found that growth is not sufficient for cells to integrate, we asked whether integra-
437 tion requires cell growth. Cell growth during the enteroblast-enterocyte transition is controlled by
438 the Tsc/Rheb/Tor pathway (Amcheslavsky et al., 2011; Kapuria et al., 2012; Nie et al., 2015; Quan et
439 al., 2013; Xiang et al., 2017). Tor pathway activation in enteroblasts can be visualized by im-
440 munostaining for the phosphorylated isoform of the Tor kinase substrate eIF4E Binding Protein
441 (phospho-4EBP) (Kapuria et al., 2012). When Tor is inactivated via overexpression of its inhibitor,
442 Tsc1/2, 4EBP is not phosphorylated (Fig. 6F) and differentiation-associated growth is blocked
443 (Kapuria et al., 2012).

444 We found that growth of SJ-less cells, like growth of normal enteroblasts, depends on Tor.
445 Phospho-4EBP immunostaining showed that *Su(H)^{ts}>sskRNAi* cells are Tor-activated, akin to *Su(H)*
446 control cells (Figs. 6D & 6E). When we conditionally overexpressed *tsc1/2* in either control cells
447 (*Su(H)^{ts}>tsc1/2*) or *ssk* knockdown cells (*Su(H)^{ts}>sskRNAi, tsc1/2*), we abrogated phospho-4EBP and
448 inhibited cell growth (Figs. 6F & 6G).

449 We next examined whether Tor inactivation and consequent growth inhibition affects the
450 ability of cells to integrate. We assessed SJ formation in *Su(H)^{ts}>tsc1/2* cells by immunostaining guts
451 for Ssk and the *Su(H)-lacZ* reporter and determining whether the Ssk signal contacted the apex of
452 β -galactosidase-labelled cells. Whereas 92% of control *Su(H)* cells formed SJs, only 53% of
453 *Su(H)^{ts}>tsc1/2* cells did (Fig. 6H). Revealingly, no *Su(H)^{ts}>tsc1/2* cells progressed beyond Stage 1 (Fig.
454 6I). Thus, SJ initiation is not sufficient for integration to progress; enteroblast growth is also neces-
455 sary. While the precise contribution of growth is currently unclear, it may fuel expansion of the um-
456 brella SJ or to initiate PAAC formation.

457 **Organ-scale impacts of blocked cellular integration**

458 Organ renewal requires that new cells integrate successfully into the epithelium. When cell
459 integration is blocked, what are consequences to organ-scale cellular equilibrium? We first asked
460 whether blocking integration causes undifferentiated cells to accumulate abnormally in the tissue
461 (Fig. 7A). When animals are maintained under stable, *ad libitum* conditions, *Su(H)⁺* cells typically
462 comprise ~10% of total cells in the midgut R4 region (Bonfini et al., 2021; O'Brien et al., 2011; Vii-
463 tanen et al., 2021). This proportion essentially doubled when we blocked integration by inhibiting
464 new SJ formation (19.1% \pm 5.5% of total cells in *Su(H)^{ts}>sskRNAi* guts; 9.3% \pm 2.8% in control guts).
465 By comparison, the proportion of *Su(H)⁺* cells remained nearly normal when we blocked integration
466 by inhibiting cell growth (12.0 \pm 2.8% in *Su(H)^{ts}>tsc1/2* guts). Concomitant inhibition of both SJ for-

467 mation and cell growth resembled growth inhibition alone ($12.0 \pm 3.2\%$ of total cells in
468 *Su(H)^{ts}>sskRNAi, tsc1/2* guts were *Su(H)-lacZ⁺*). Thus, whether integration-blocked cells accumulate
469 in the tissue depends on the means through which integration was blocked. One possible reason
470 may be differences in differentiation state of the integration-blocked cells. Early-stage enteroblasts,
471 which still adhere strongly to their mother stem cell, can repress subsequent mother cell divisions
472 (Choi et al., 2011), and *Tsc1/2* overexpression – but not SJ inhibition – arrests differentiation at an
473 early stage ((Kapuria et al., 2012) and Figs. 6C & S5C-G). This early-stage arrest may enable growth-
474 inhibited cells to repress production of additional daughter cells.

475 We next examined whether blocking integration alters the organ's total number of cells (Fig
476 7B). Comprehensive counts of DAPI-labeled nuclei in the midgut R4ab region revealed that total cell
477 number remains normal when new cells cannot integrate, even for guts in which integration-
478 blocked cells accumulate abnormally (1997 ± 489 cells in control *Su(H)^{ts}* guts compared 1960 ± 398 ,
479 2067 ± 210 cells, and 1611 ± 299 cells in *Su(H)^{ts}>sskRNAi*, *Su(H)^{ts}>tsc1/2*, and *Su(H)^{ts}>sskRNAi, tsc1/2*
480 guts, respectively). We speculate that feedback mechanisms inherent to organ-scale control of total
481 cell number (Akagi et al., 2018; Jin et al., 2017; Liang et al., 2017) 'sense' unintegrated cells and exert
482 a compensatory effect on cellular equilibrium.

483 DISCUSSION

484 Epithelial organs maintain a leakproof barrier between the interior body and the external en-
485 vironment even while continuously replacing the cells that directly contact this environment. In
486 many barrier epithelia, these replacement cells derive from basal stem cells and are born without a
487 luminal-apical surface or occluding junctions, two structures that are essential for barrier integrity.
488 Consequently, daughters must generate these structures *de novo* and integrate into the barrier as
489 they differentiate.

490 We examined this process at ultra-fine spatial resolution during physiological turnover of
491 the *Drosophila* intestinal epithelium. Our analyses led to a previously undescribed mechanism that
492 we term PAAC-mediated integration (Fig. 7C): The new cell forms a broad, umbrella-shaped SJ that
493 serves as a transient niche for biogenesis of the cell's future luminal-apical surface (the PAAC).
494 When the new cell is sufficiently mature, the umbrella SJ retracts and the PAAC lumen fuses with
495 the gut lumen, exposing the cell's apical membrane to the external environment. In contrast to a pri-
496 or model of radial intercalation (Fig. 7C), PAAC-mediated integration enables stem cell daughters to
497 form barrier structures in a space sheltered from the contents of the gut lumen – a potentially crucial

498 safeguard for an epithelium that is simultaneously physiologically active and continuously renew-
499 ing.

500 **PAAC architecture: Implications for epithelial lumen formation**

501 Lumens are defining features of epithelial tubes, and the molecular and cellular events that
502 drive lumen formation are a topic of intense interest. Our current understanding of lumen formation
503 comes from studying epithelial cells that are at similar states of differentiation (Blasky et al., 2015;
504 Datta et al., 2011; Overeem et al., 2015; Sigurbjörnsdóttir et al., 2014). PAACs provide a first, fine-
505 grained example of how lumens form between cells that are at disparate states of differentiation.
506 This fate difference likely underlies the PAACs' two distinctive characteristics, structural asymmetry
507 and split polarity. Below, we speculate how these PAAC-specific characteristics may shed new light
508 on lumen-forming mechanisms in general.

509 PAACs are, to the extent we can determine, the first type of intercellular lumen that exhibits
510 split polarity--the membranes that form PAACs alternate between apical identity (the pre-
511 enterocyte) and basolateral identity (mature enterocytes) (Figs. 3, 5 & 7C; and Video 6). By compari-
512 son, all epithelial lumens of which we are aware are normally enclosed by membranes that are ex-
513 clusively apical (Blasky et al., 2015; Datta et al., 2011; Overeem et al., 2015; Sigurbjörnsdóttir et al.,
514 2014). Our finding that PAACs' mature enterocyte membranes do not form a secondary apical do-
515 main is surprising because cells that contact multiple lumens in developing epithelia form a corre-
516 sponding apical domain for each lumen (Alvers et al., 2014; Bagnat et al., 2007; Bryant et al., 2010).
517 One possible explanation is that terminally differentiated epithelial cells actively repress secondary
518 apical domains whereas epithelial cells in developmental contexts do not. Another, non-exclusive,
519 possibility is that all lumens transiently exhibit split apical/basal polarity at their earliest stage -- one
520 lumen-forming cell initiates an apical domain prior to the others -- but that this stage is, in most cas-
521 es, extremely short-lived, so it has not been detected previously.

522 PAACs' second striking feature is their extreme structural asymmetry: pre- and mature en-
523 terocyte membranes, despite being bonded at their edges by the same SJ, acquire shapes that are ex-
524 treme opposites. The pre-enterocyte PAAC membrane, which grows dramatically and invaginates
525 deeply into the cytoplasm of the differentiating cell, convolutes into sharp folds and broad curves.
526 This structure, which is superimposed onto the membrane's fine-scale microvillar folds, sets the
527 volume of the PAAC. The mature enterocyte membranes, by contrast, appear largely passive. They
528 sit like a lid atop the neck of the pre-enterocyte invagination and do not appear to morph or expand
529 during differentiation (*e.g.*, compare the nascent and advanced PAACs in Fig. 5 and Video 6).

530 These two features, split apical/basolateral polarity and structural asymmetry, provide in-
531 sight into opposing models of lumen formation. The structural asymmetry of PAACs is incompati-
532 ble with the prevailing model of lumen formation, in which hydrostatic pressure drives lumen
533 growth (Chan et al., 2019; Dasgupta et al., 2018; Dumortier et al., 2019; Ruiz-Herrero et al., 2017;
534 Yang et al., 2021), because lumens generated by hydrostatic pressure are uniformly convex (Vasquez
535 et al., 2021). Rather, this asymmetry evokes a recently proposed alternative mechanism in which ex-
536 pansion of apical membrane surface drives lumen growth in a pressure-independent manner
537 (Vasquez et al., 2021). Indeed, since growth of the PAAC lumen is accounted for by apical surface
538 expansion of a single cell, PAACs may provide an informative case study of apical surface-driven
539 growth. Identifying the molecular signals that target and stabilize new PAACs will aid in exploring
540 these scenarios.

541 **A trade-off between barrier integrity and junction-forming efficiency**

542 In both PAAC-mediated integration and radial intercalation, single cells assimilate into an
543 epithelium through basal-to-apical movement. Why do distinct mechanisms exist to reach the same
544 cellular endpoint? We speculate that, in general, basal-to-apical assimilation requires a trade-off be-
545 tween integration speed and barrier integrity. A given mechanism may favor one of these qualities
546 at the expense of the other. In principle, a spectrum of mechanisms enables tissues to employ the
547 mechanism that is best suited to their specific biological context.

548 In this schema, radial intercalation is rapid and parsimonious. It occurs over time scales of
549 minutes or a few hours. New junctions initiate within the pre-existing junctional network and ex-
550 pand directly into their final morphology, an apico-lateral band. Intriguingly, all examples of radial
551 intercalation described in the literature take place in developing epithelia (Merzdorf et al., 1998;
552 Deblandre et al., 1999; Stubbs et al., 2006; Voiculescu et al., 2007; McMahon et al., 2008; Campbell et
553 al., 2010). Because embryos themselves are housed in a protective environment (such as an egg or a
554 womb), cells in embryonic tissues can display immature junctions and incipient microvilli at the or-
555 gan's apical surface without risking exposure to the external environment.

556 PAAC-mediated integration is slower and, since it involves building and then retracting a
557 temporary scaffold, likely less efficient. We estimate that typical time frames for PAAC-mediated
558 integration are >24 h, based on changes in nuclear size of stem cell daughters over time (Koyama et
559 al., 2020). (Indeed, this >24 h time frame presented a challenge for Windowmount live imaging,
560 which typically yields movies ~8-20 h in duration.) A differentiating cell may require this time to
561 construct the umbrella SJ and microvilli-lined PAAC – large structures that will undergo extensive

562 remodeling in subsequent stages. The indirect, more complex nature of PAAC-mediated integration
563 provides an additional layer of protection for differentiating cells—a potentially worthwhile tradeoff
564 for a functionally active organ that continuously processes substances from the external environ-
565 ment.

566 How do SJs guide differentiating cells into the epithelial sheet? One appealing notion is that
567 they exert myosin-based pulling forces that draw differentiating cells toward the lumen
568 (Varadarajan et al., 2019; Yu and Zallen, 2020). We were, however, unable to identify any impact on
569 integration following enteroblast-specific inhibition of Rho kinase (Rok; data not shown). Since Rok
570 is an essential activator of myosin contractility, this finding implies that myosin-based forces are not
571 required in the integrating cell. A second possibility is that myosin-based pulling forces, or some
572 other cytoskeletal regulator, is required in mature neighbor cells to aid the basal-to-apical movement
573 of differentiating cells. Since SJs bond together mature and differentiating cells, they are well-
574 positioned to coordinate these two cell types during integration. Finally, SJs may serve to polarize
575 growth and/or cytoskeletal assembly along the apical-basal axis of the differentiating cell (Madara,
576 1987).

577 **Diverse epithelial architectures may use a diversity of cell assimilation mechanisms**

578 Numerous barrier epithelia, including mammalian trachea, cornea, and olfactory lining, have
579 a cellular organization similar to the fly gut (Chepko and Dickson, 2003; Chepko and Smith, 1997;
580 Cotsarelis et al., 1989; Evans and Moller, 1991; Leung et al., 2007; Michael J. Evans, 2001; Rock et al.,
581 2009; Sekiya et al., 1988; Tsujimura et al., 2002). All these tissues are renewed by basally localized
582 stem cells that lack occluding junctions and lumenal-apical surfaces. Their daughter cells thus all
583 face the same architectural challenge of integrating seamlessly into the barrier while they differenti-
584 ate. Whether they overcome this challenge through PAAC-mediated integration, like the fly gut, or
585 through some other, perhaps as-yet-undefined, mechanism will be an interesting question for future
586 investigation.

587 In considering how epithelial architecture affects new cell integration, it is notable that two
588 of the best-understood barrier epithelia, mammalian intestine and lung alveoli, sidestep the chal-
589 lenge of barrier integration entirely. In these tissues, stem cells possess both occluding junctions and
590 lumenal-apical surfaces, and daughter cells symmetrically inherit these structures from their mother
591 (Fig. 7C) (DeMaio et al., 2009; Fleming et al., 2007; Jinguji and Ishikawa, 1992; McKinley et al., 2018).
592 Symmetric inheritance is morphogenetically parsimonious, but it requires the abscission of existing
593 junctional septa and creation of new septa at the new daughter-daughter interface. Since this re-

594 modeling happens at the luminal surface, it might produce potential weak points in the barrier.
595 Thus, at first glance, the fact that mammalian intestine and lung use symmetric inheritance to assim-
596 ilate new cells seems at odds with the idea that physiologically active epithelia need extra safe-
597 guards to protect barrier integrity.

598 We speculate, however, that this potential risk is mitigated by these tissues' particular archi-
599 tecture; namely, deeply recessed niches – intestinal crypts and terminal alveolar endbuds – in which
600 the lumen-exposed stem cells reside. Crypts and endbuds are secluded from bulk luminal flow,
601 which provides their resident stem cells with built-in protection that stem cells in other epithelia
602 lack. This built-in protection conceivably affords stem cell daughters the simplicity of directly inher-
603 iting barrier structures from their mother cell. In this light, PAACs may be seen as a cellular-scale
604 solution for epithelia that lack recessed stem cell niches, the tissue-scale solution for protecting new
605 cells. As such, our findings spotlight the intimate relationship between physiological function, organ
606 form, and cellular differentiation and morphogenesis.

607

608 MATERIALS and METHODS

609 **Drosophila husbandry**

610 Mated adult female flies were used in all experiments. Crosses utilizing the TARGET system
611 (GAL4/GAL80^{ts}) were performed at 18°C (McGuire et al., 2003). Upon eclosion, adult animals were
612 temperature shifted to 29°C for 4 days to inactivate GAL80^{ts} and induce GAL4-mediated expression.
613 Midguts were harvested for immunostaining 4 days after induction. Flies used for immunofluores-
614 cence were raised on standard molasses medium at 18°C. Upon eclosion, they were shifted to 29°C.
615 Midguts were harvested for immunostaining 4 days after eclosion.

616 **Immunohistochemistry and sample preparation for confocal microscopy**

617 Dissected guts were fixed in 4% formaldehyde in PBS (pH 7.4) at room temperature for 1
618 hour, immunostained, and mounted as previously described (O'Brien et al., 2011). Primary antibod-
619 ies: mouse anti-Armadillo (1:100, DSHB N2 7A1), rabbit anti-Snakeskin (1:1000, gift from Furuse lab),
620 mouse anti-Coracle (1:50, DSHB C615.16), mouse anti- β -galactosidase (1:400, Promega Z3781), rabbit
621 anti-Phospho4EBP1 (1:500, Cell Signaling). Secondary antibodies: donkey anti-rabbit IgG conjugated
622 to Alexa 555 and donkey anti-mouse IgG conjugated to Alexa 647 (1:1000, Invitrogen A-31572 and
623 A-31571, respectively). Nuclei were stained with DAPI (LifeTechnologies D1306). Samples were in-
624 cubated with primary antibody overnight at 4°C in PBT (PBS with 3% Triton X-100 (Sigma-Aldrich
625 X100-100 mL)) with 5% NGS (Capralogics GS0250), washed 3 times in PBT, then incubated with sec-
626 ondary antibody for 4 hours at room temperature in PBT with 5% NGS. Samples were mounted in
627 ProLong (LifeTechnologies P36984) and stored at -20°C until imaging.

628 **Induction of MARCM clones**

629 Heat-shock MARCM clones (Lee and Luo, 1999) were generated by collecting adult flies 12-
630 24 hours post-eclosion and performing two 45-min, 37°C heat shocks separated by a 8-min chill on
631 ice. Flies were returned to 25°C for 4 days, then dissected and analysed.

632 **Fixed sample imaging**

633 Fixed samples were imaged on a Leica SP8 WLL confocal microscope with a 63x HC PL APO
634 CS2 oil objective. Serial optical sections were taken at 0.5 μ m intervals through the entirety of whole-
635 mounted, immunostained midguts.

636 **Quantitation of SJ-contacting and non-contacting cells**

637 Enteroblasts in the midgut R4ab region (also known as P1/2) (Buchon et al., 2013; Marianes
638 and Spradling, 2013; O'Brien, 2013) were visualized and counted using ImageJ/Fiji (Schindelin et al.,
639 2012). The R4ab region was identified using morphological landmarks. SJs were identified by im-
640 munostaining for the SJ component Snakeskin. Su(H)-lacZ⁺ (β -Gal⁺) cells were recognized as entero-
641 blasts by visual inspection. To categorize enteroblasts as SJ-contacting or non-contacting, each enter-
642 oblast was analyzed through Fiji Orthogonal View. Enteroblasts were defined as SJ-contacting cells

643 if the β -Gal⁺ signal was juxtaposed and/or displayed overlap with apical Snakeskin signal in XY, XZ
644 and YZ planes. Enteroblasts were defined as SJ non-contacting cells if they lacked these criteria.

645 **Measurements of cell volume**

646 To measure volumes of *Su(H)-lacZ*⁺ cells, tissues were fixed, immunostained using anti- β -
647 galactosidase antibody, mounted, and subjected to volumetric confocal imaging. After initial pro-
648 cessing in Fiji, files were imported to Bitplane Imaris v.8.7. Volumes of *Su(H)-lacZ*⁺ cells were deter-
649 mined by creating a surface for each cell using the Imaris contour tool and then measuring the en-
650 closed volume.

651 **Ovary dissection and staining**

652 Egg chambers were dissected in phosphate-buffered saline (PBS pH 7.4) + 0.1% Triton X-100
653 and incubated for 2 hours in 1mM latrunculin B (LatB; Sigma). They were then fixed 20 min in 4%
654 PFA (in PBS pH 7.4), incubated 2 hours in a 1:250 dilution of TRITC-conjugated phalloidin (Molecu-
655 lar Probes, Eugene, OR), and subsequently imaged on a Zeiss LSM 700 confocal microscope.

656 **Total cell and total enteroblast counts**

657 To perform total cell counts and total enteroblast counts of R4ab, confocal image stacks were
658 digitally isolated in Fiji. Bitplane Imaris was used generate three-dimensional organ reconstructions,
659 and individual cells were comprehensively counted by mapping signals for DAPI (for total cell
660 counts) or *Su(H)-lacZ* (for total enteroblast counts) to Imaris surface objects. Imaris-recognized sur-
661 faces were confirmed through visual inspection and manually adjusted when needed for accuracy.

662 ***In vivo* live imaging and movie analyses**

663 Live imaging was performed on 2-3 day old adult females as described previously (Martin et
664 al., 2018), with the following modifications: For Video 4, 20 nM RU486 and 10 μ g/mL Isradipine
665 were added to the imaging media to induce GeneSwitch5966 expression and reduce intestinal peri-
666 stalsis, respectively. For Video 5, 10 μ g/mL Isradipine was added to the imaging media to reduce
667 intestinal peristalsis.

668 Videos were acquired with a LSM Leica SP5 with a HCX APO L 20x/ 1.00W lens, controlled
669 by LAS AF software. Confocal sections were taken every 15 mins with z-steps of 1.01 μ m (Video 4)
670 and 2.98 μ m (Video 5). Videos were processed on a Windows computer (Windows 10 Education)
671 with a 3.70 GHz quad-core Intel Xeon processor and 256 GB memory. Videos were initially pro-
672 cessed in Fiji and subsequently visualized in volumetric format and analyzed in Bitplane Imaris. For
673 Video 4, the following Fiji plugins were applied: 1) Stack Sorter ([https://www.optinav.info/Stack-
674 Sorter.htm](https://www.optinav.info/Stack-Sorter.htm)), to correct the alignment of out-of-order slices captured during a peristaltic contraction,
675 2) StackReg (Arganda-Carreras et al., 2006) to correct for whole-organ X-Y movements, 3) Correct 3D
676 Drift (Parslow et al., 2014) to correct for global volume movements, and 4) TrakEM2 (Cardona et al.,
677 2012) to perform manual X-Y alignment for slices that could not be registered automatically. The lat-
678 ter 3 plugins were applied iteratively as needed. For Video 5, Stack Sorter, StackRed, and Correct 3D
679 Drift were used. The latter two plugins were applied iteratively as needed.

680 **Measurements of cross-sectional cell area in live movies**

681 The cross-sectional area of the integrating Su(H)-mCherry⁺ cell at each timepoint in Video 4
682 was determined as follows: The cell's largest cross-sectional plane at each time point was identified
683 by visual inspection. FIJI Measure was used to manually outline the mCherry signal in this plane
684 and to measure the enclosed area.

685 **Sample preparation for FIB-SEM**

686 Fly guts were dissected in PBS and immediately processed as previously described (Daniel et
687 al., 2018; Kolotuev, 2014). Briefly, the samples were fixed in 1% formaldehyde, 2.5% glutaraldehyde
688 in 0.1M phosphate buffer (PB) for 2 hours at room temperature, then incubated for 1 hour in 2%
689 (wt/vol) osmium tetroxide and 1.5% (wt/vol) K₄[Fe(CN)₆] in PB followed by 1 hour in 1% (wt/vol)
690 tannic acid in 100 mM cacodylate buffer, then 30 minutes in 2% (wt/vol) osmium tetroxide in water
691 followed by 1% (wt/vol) uranyl acetate for 2 hours at room temperature. After the dehydration cy-
692 cles, samples were embedded in Epon-Araldite mix. Samples were flat embedded to assure the tar-
693 geting of the region of Interest during the sectioning step.

694 **Sample preparation for CLEM**

695 To preserve native fluorescence for correlative light/electron microscopy, samples were sub-
696 jected to high-pressure freezing followed by rapid freeze-substitution, as previously described
697 (Kolotuev, 2014; Kolotuev et al., 2010). Dissected guts were immediately transferred to large high
698 pressure freezing carriers filled with 20% bovine serum albumin for cryo-protection and frozen us-
699 ing the standard procedure according to the manufacturer's instructions (High Pressure Freezing
700 Machine HPF Compact 02, Engineering Office M. Wohlwend GmbH, Sennwald, Switzerland). Sam-
701 ples were substituted in an AFS2 machine (Leica) with 0.1% uranyl acetate diluted in anhydrous ace-
702 tone and embedded in HM20 acrylic resin mix (Electron Microscopy Sciences). To assure precise
703 orientation of the samples, the flat embedding procedure was used (Kolotuev, 2014).

704 **Electron microscopy image acquisition and analysis**

705 Polymerized flat blocks were trimmed using a 90° diamond trim tool (Diatome, Biel, Switzer-
706 land) mounted on a Leica UC6 microtome. Transmission electron microscopy samples were ana-
707 lyzed with an FEI CM100 electron microscope operated at 80kV, equipped with a TVIPS camera pi-
708 loted by the EMTVIPS program.

709 Samples for CLEM were sectioned at 100-150 nm thickness and transferred to wafers using
710 an array tomography protocol (Burel et al., 2018; Kolotuev and Micheva, 2019). CLEM wafers were
711 first imaged for fluorescence signal using a Zeiss fluorescent microscope equipped with DAPI and
712 GFP filters using 20x and 60x objectives. To analyze the ultrastructure, sections on wafer were con-
713 trasted with uranyl acetate and lead citrate and observed using an FEI Quanta 250 FEG scanning
714 electron microscope (FEI, Eindhoven). The imaging settings were as follows: accelerating voltage,
715 10kV; spot size, 5; image dimensions, 4096x4096; pixel dwell time, 10μs.

716 FIB-SEM tomography was done with a Helios 650 (FEI, Eindhoven). FIBbing conditions were
717 30 keV, 770 pA, 30-40 nm slice thickness (specified in text for each experiment) at a tilt angle of 52°

718 and a working distance of 13 mm. For imaging the block face was tilted normal towards the electron
719 beam (Kizilyaprak et al., 2015). The imaging conditions were: 2 keV, 800 pA, 20 μ s dwell time, with a
720 frame size of 6144 x 4096 and a pixel size of 9.7 nm. For publication, the image contrast was invert-
721 ed.

722 IMOD (Kremer et al., 1996) was used to convert raw data from sequential sections to an MRC
723 file stack and also used for alignment of serial sections and volumetric rendering. Adobe Photoshop
724 was used for image adjustment, layers superposition, annotations, pseudo-coloring of image zones,
725 and volume reconstructions.

726 **Volumetric rendering of FIB-SEM images**

727 Serial sections were stacked and aligned using the cross-correlation function of IMOD, which
728 was also used to trace and reconstruct specific regions. Drawing tools were used for outlining sub-
729 cellular features (e.g., septate junctions, plasma membrane, nuclei, PAAC) on the EM layers. The 3D
730 reconstruction surfaces were Meshed in Model View/ Objects tool. Images were captured using the
731 Model View/Movie Montage tool and reformatted into .avi format using Fiji.

732

733 **FUNDING SOURCES**

734 P.M.R. was supported by a Stanford Bio-X Bowes Graduate Fellowship, an EMBO Short-
735 Term Travelling Fellowship, and a Stanford DARE Graduate Fellowship (Diversifying Academia,
736 Recruiting Excellence). The authors acknowledge the financial support by the Faculty of Biology and
737 Medicine of the University of Lausanne and of the Swiss National Science Foundation, R'Equip
738 Grant 316030_128692. This work was supported by NIH R01GM116000-01A1, NIH R35GM141885-01,
739 and ACS RSG-17-167-01 to L.E.O.

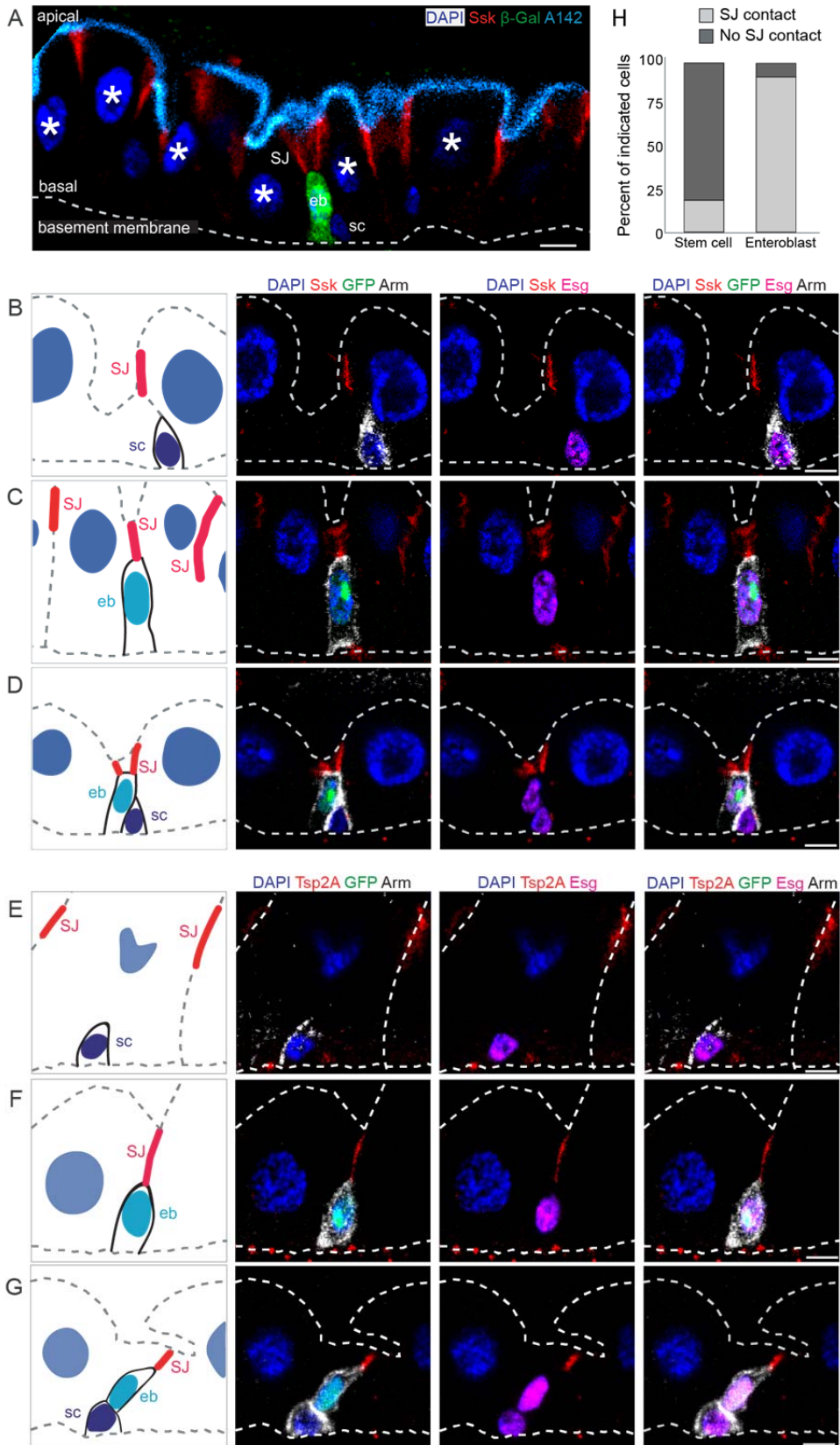
740 **ACKNOWLEDGEMENTS**

741 We are grateful to Allison Bardin, David Bilder, Nicolas Buchon, Joaquin de Navascues, Mik-
742 io Furuse, Yoshihiro Inoue, Henri Jasper, Sarah Siegrist, Norbert Perrimon, Nicolas Tapon, Charles
743 Xu, and Drosophila stock centers (Bloomington *Drosophila* Stock Center (NIH P40OD018537), Vienna
744 *Drosophila* Resource Center (Dietzl et al., 2007), Kyoto *Drosophila* Genomics and Genetic
745 Resources) for fly stocks; Mikio Furuse, Claire Thomas, Steven Russell, and Xiaohang Yang for anti-
746 bodies; and Jon Mulholland and Kitty Lee for microscopy support. Confocal microscopy was per-
747 formed at the Stanford Beckman Cell Sciences Imaging Facility (NIH 1S10OD01058001A1, NIH
748 1S10OD010580). We thank David Bryant, Tobias Reiff, Daniel St. Johnston, Jia Chen, and members
749 of the O'Brien lab for invaluable discussions. Fly extract was obtained from the *Drosophila* Genomics
750 Resource Center (NIH 2P40OD010949).

751

752

754 **Figure 1**



756 **Figure 1. The apical tip of a differentiating enteroblast contacts the SJ of its neighbor en-**
757 **terocytes.**

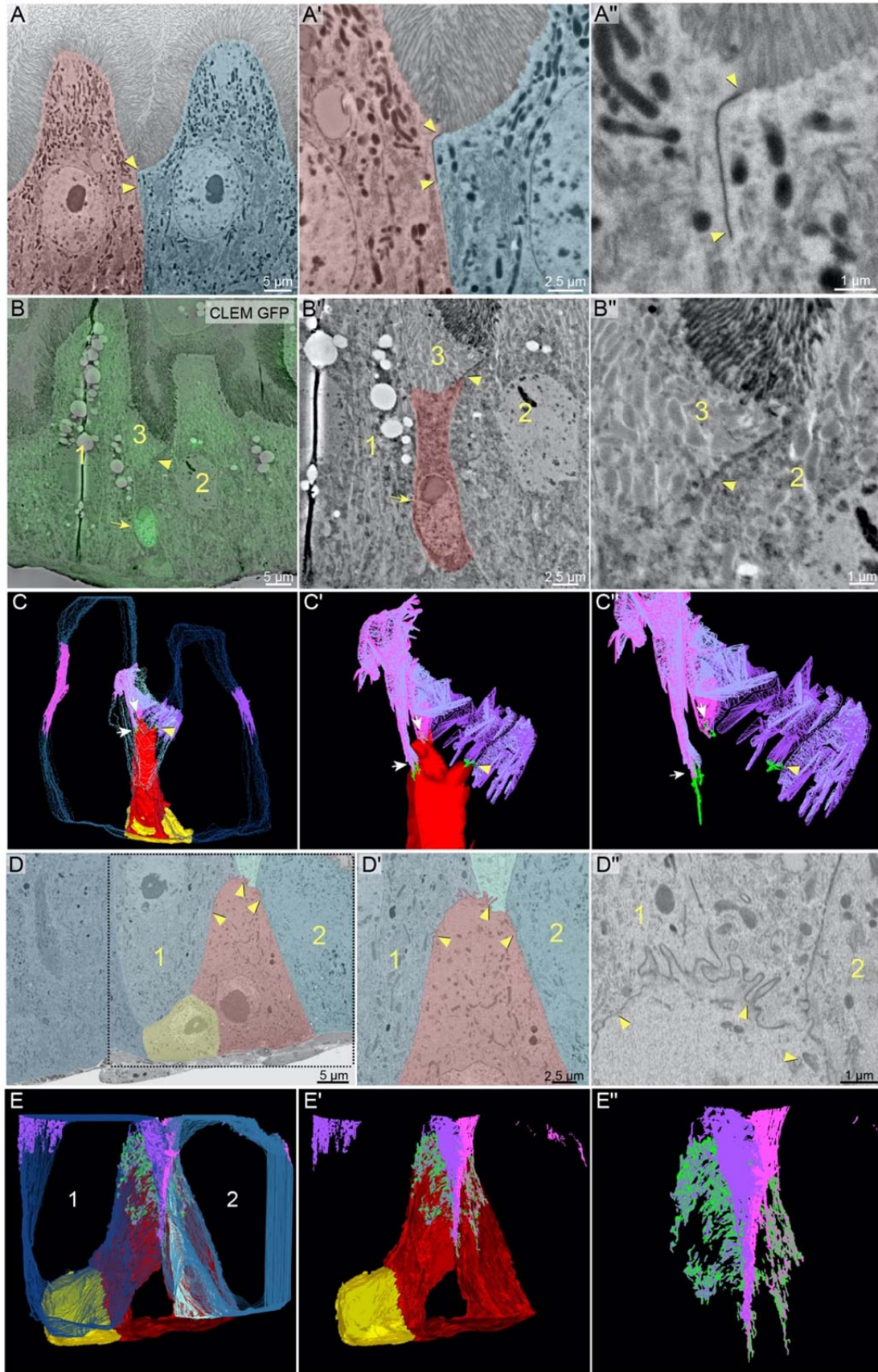
758 (A) Architecture and stem cell lineage of the fly midgut epithelium, shown in cross-sectional
759 view with apical luminal surface (cyan, Mdu::GFP; *c.f.* Fig. S2) at top and basal surface (dotted line,
760 basement membrane) at bottom. Three cell types make up the absorptive lineage: (1) Stem cells (sc)
761 are basally localized, diploid cells that do not express *Su(H)-lacZ*. (2) Enteroblasts (eb) are terminally
762 committed stem cell progeny. Enteroblasts are transitioning from stem-like cells to enterocytes and
763 are marked by *Su(H)-lacZ* expression (green, β -Gal). Stem cells and enteroblasts often appear in pairs.
764 (3) Mature enterocytes are large cells with polyploid nuclei (asterisks). Septate junctions (SJ; red,
765 Snakeskin) appear at the apico-lateral borders of enterocytes.

766 (B-G) Stem cells do not overlap with SJs, while the apical tips of enteroblasts contact the basal
767 termini of enterocyte-enterocyte SJs. Cartoons (left column) and channel overlays from 5-channel
768 multi-photon laser microscopy of *esgGAL4, UAS-his2b::CFP; Su(H)-GFP:nls* midguts immunostained
769 for SJ components Ssk (red, B-D) or Tsp2a (red, E-G) and for the stem cell/enteroblast marker Arm
770 (white; cortical). *esg*-driven His2b::CFP is shown in magenta, *Su(H)*-driven GFP:nls in green and nu-
771 clei (DAPI) in blue. Luminal epithelial surface and basement membrane are indicated by dotted
772 gray lines. Stem cells (sc) are His::CFP⁺, Arm⁺, GFP:nls⁻ cells in Panels B, D, E, G; enteroblasts (eb)
773 are His::CFP⁺, Arm⁺, GFP:nls⁺ cells in Panels C, D, F, G. Panels D and G show stem cell-enteroblast
774 pairs. All scale bars: 5 μ m. Images are projections of short confocal stacks. Full genotypes in Table 1.

775 (H) Quantitation of B-G. Most enteroblasts (92%), but few stem cells (19%) contact the epithe-
776 lial septate junction network. N=5 midguts; n=119 stem cells and 125 enteroblasts.

777

Figure 2



781 **Figure 2. The differentiating enteroblast's apex initiates a new SJ at the basal-most edge**
782 **of mature enterocyte SJs and triggers their remodeling to form a basally-extended SJ**
783 **sheet.**

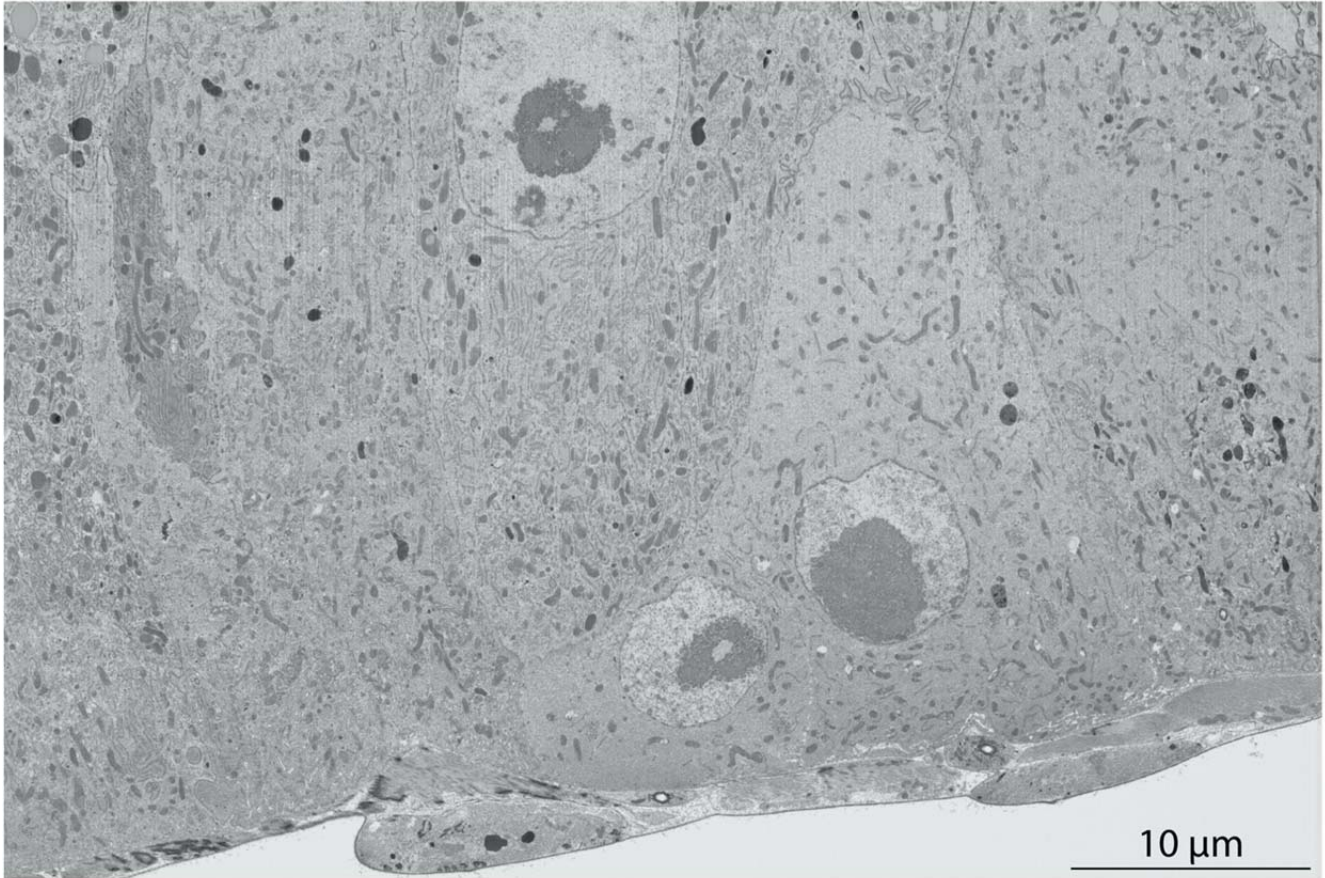
784 (A) Mature enterocytes localize SJs to the boundary between lumen-facing, brush border api-
785 cal membranes and lateral membranes. SEM shows two mature enterocytes (pink and blue pseudo-
786 color). Apical membranes are identifiable as microvilli-rich brush borders. An electron-dense SJ (ar-
787 rowheads) fuses together the enterocytes' lateral membranes at a site directly adjacent to these brush
788 borders. Zoomed-in views of SJ in A are shown in A' and A''.

789 (B-C) The apex (apical-most tip) of a young, Su(H)⁺ enteroblast initiates SJ adhesions at the
790 basal edge of enterocyte SJs. CLEM overlay (B) identifies a Su(H)-GFP::nls⁺ enteroblast (arrow) in a
791 FIB- SEM section. Zoomed-in images of the enteroblast (B', red pseudocolor) and of the enteroblast
792 apex (B'') show a nascent SJ (arrowheads in B-B'') between the enteroblast and neighbor enterocytes
793 2 and 3 (labelled). (Only a small wedge of enterocyte 3 is visible in this section.) See Fig. S1. Volu-
794 metric rendering (C) of 30 FIB-SEM sections, including the section in B, reveals that each of apex's
795 three fingers forms a SJ (arrows and arrowhead; arrowhead points to the same SJ in B and C) with
796 each of three neighbor enterocytes. Cells and SJs are color coded: enteroblast, red; enteroblast SJs,
797 green; enterocytes 1-3, blue; enterocyte 1 SJs, magenta; enterocyte 2 SJs, light purple; enterocyte 3 SJs,
798 light blue; stem cell, yellow. Zoomed-in views of the enteroblast apex and associated SJs are shown
799 in C' and C''. See Video 1.

800 (D-E) An older enteroblast is blanketed by the broad, basally extended SJ it has formed with
801 the lateral membranes of neighboring mature cells. A FIB-SEM section (D) shows an enteroblast (red
802 pseudocolor), two mature enterocytes (cells 1 and 2; blue pseudocolor), a mature enteroendocrine
803 cell (cell 3; light blue pseudocolor), and a presumptive stem cell (yellow pseudocolor). The apical
804 third of the enteroblast has formed an SJ (arrowheads in D-D'') with the lateral membranes of the
805 mature cells. Zoomed-in views of the enteroblast apex are shown in D' and D''. Volumetric render-
806 ing (E) of 413 FIB-SEM sections, including the section in D, reveals basal extensions of both entero-
807 blast-enterocyte SJs and associated enterocyte-enterocyte SJs. View of the SJ with only the entero-
808 blast and stem cell is shown in E'. Zoomed-in view of the SJ alone is shown in E''. Cells and SJs are
809 color coded: enteroblast, red; enteroblast SJ, green; enterocytes 1 and 2, blue; enterocyte 1 SJ, laven-
810 der; enterocyte 2 SJ, magenta; enteroendocrine cell, light blue; stem cell, yellow. See Video 2. Full
811 genotypes in Table 1.

812

813 **Figure S1 (related to Figure 2C)**



814

815 **Figure S1 (related to Figure 2D). High resolution view of FIB-SEM section shown in Fig-**
816 **ure 2D.**

817 30 nm-thick sections were cut with a gallium ion beam at 30 keV and 770 pA. Images were
818 taken with the electron beam at 2 keV, 0.8 nA, 2 mm working distance, 20 μ s dwell time, 6144x4096
819 pixel frame size. Pixel size 9.7nm. Full genotypes in Table 1.

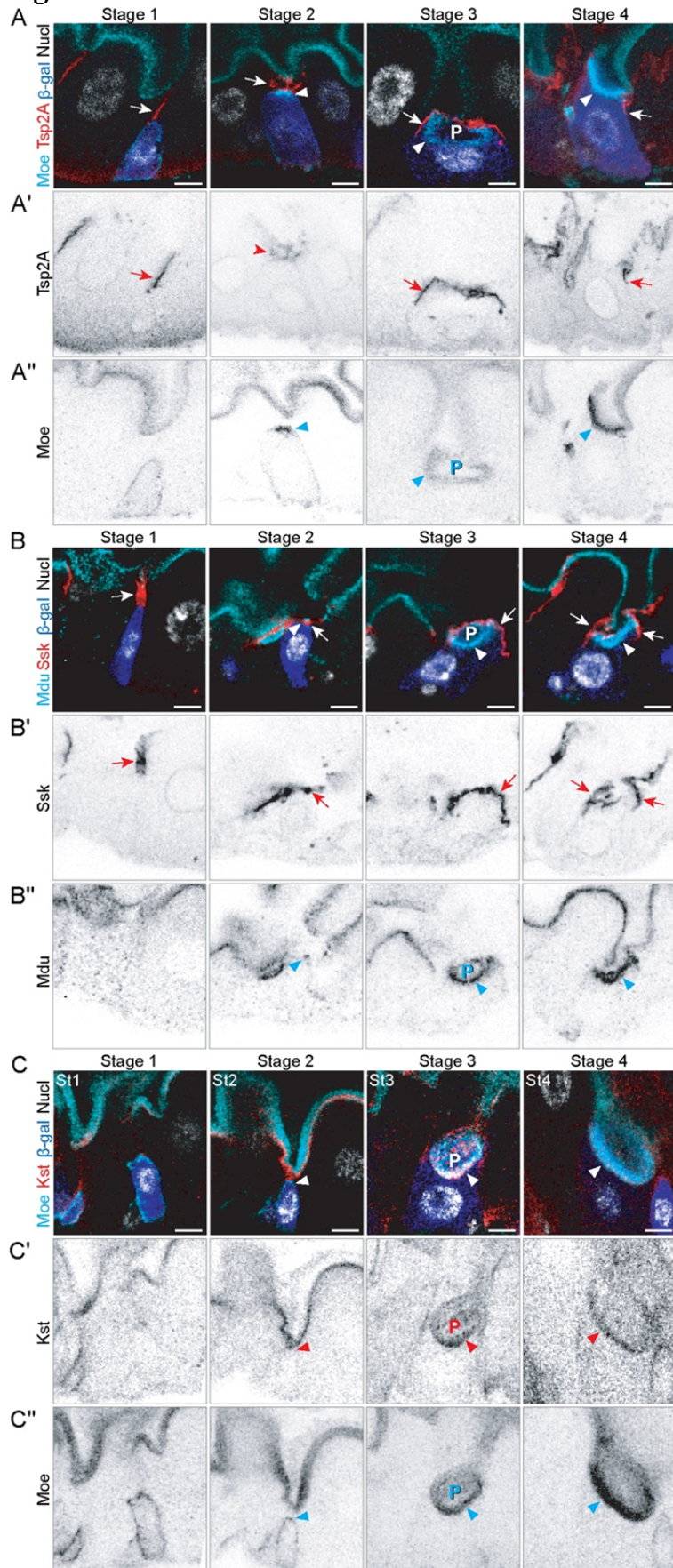
820 **Video 1 (related to Figure 2C). Three-dimensional ultrastructure of nascent SJ between**
821 **Su(H)-GFP::*nls*⁺ enteroblast and mature enterocytes.**

822 Tomographic reconstruction of 30 serial images, including the image in Fig. 2B, from midgut
823 expressing *Su(H)-GFP::*nls**. Serial sections were cut with a gallium ion beam at 10kV, spot size 5, pix-
824 el frame size 4096x4096, pixel dwell time 10 μ s. Pixel size 8.7nm. Slice thickness, 150nm. Volume of
825 reconstruction, 35.6 μ m x 35.6 μ m x 4.5 μ m. Full genotypes in Table 1.

826 **Video 2 (related to Figure 2E). Three-dimensional ultrastructure of SJ 'cap' between en-**
827 **teroblast and mature cells.**

828 Tomographic reconstruction of 413 serial FIB-SEM images, including the image shown in
829 Figs. 2C and S1. Volume of reconstruction, 55 μ m x 36.6 μ m x 12.3 μ m. Slice thickness, 30nm. Full
830 genotypes in Table 1.

831

Figure 3

834 **Figure 3. SJ and apical membrane morphology define four stages of barrier integration.**

835 As differentiating cells integrate, they pass through four morphological stages that are dis-
836 tinguishable by SJ localization, polarization of apical markers, and cellular/ nuclear size. SJs shown
837 in red (A, Tsp2A; B, Ssk). Markers of enterocyte apical polarity shown in either cyan (A, C Moe::GFP;
838 B, Mdu::GFP; *c.f.* Fig. S2) or red (C, Kst). Su(H)-lacZ in blue (β -Gal, A-C). Nuclei (Nucl) shown in
839 grayscale (A, Stage 1 and C - His2av::mRFP; A, Stages 2-4 and B - DAPI). Images are projections of
840 short confocal stacks. Markers that are not fused to a fluorescent protein were visualized by im-
841 munostaining. All scale bars, 5 μ m. β -gal channel shown in Fig. S3. Full genotypes in Table 1.

842 Stage 1 (St1). Enteroblast with initial SJ contact. The apex of a diploid enteroblast contacts the
843 basal terminus of an enterocyte-enterocyte SJ (arrows). Apical markers are either non-polarized
844 (Moe, Kst) or absent (Mdu).

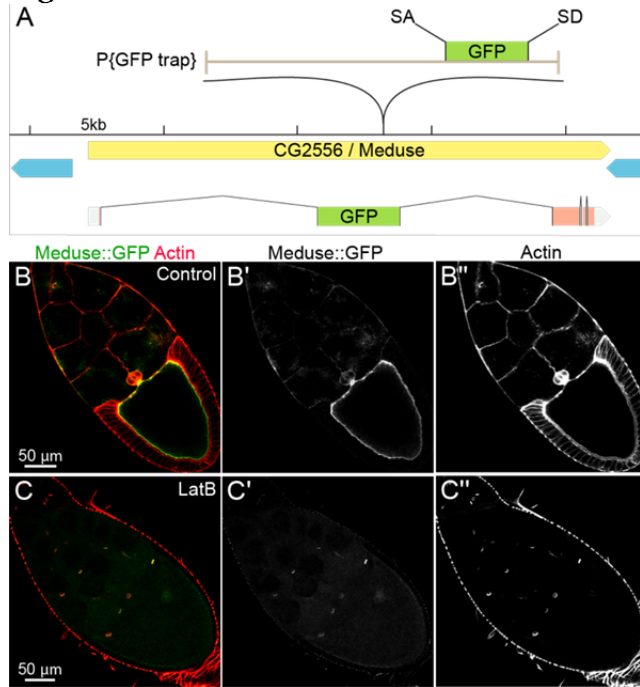
845 Stage 2 (St2). Enteroblast with broadened SJ contacts and apical plaque. The enteroblast apex
846 is partially covered by a widened enteroblast-enterocyte SJ (arrows). Some apical markers (Moe,
847 Mdu; arrowheads) become polarized to the apex, forming a plaque immediately basal to the SJ.

848 Stage 3 (St3). Pre-enterocyte with umbrella-like SJ and concave apical structure (PAAC). The
849 apex of the cell is fully covered by a convex SJ (arrows). Apical markers outline a prominent concave
850 structure (P; Pre-Assembled Apical Compartment, or PAAC) beneath the SJ. The PAAC fills the
851 apex of the cell and is separate from the gut lumen (Video 3). Pre-enterocytes exhibit cytoplas-
852 mic/ nuclear sizes intermediate between enteroblasts and mature enterocytes and low *Su(H)*-driven
853 β -gal signal (Fig. S3).

854 Stage 4 (St4). Pre-enterocyte integration becomes complete. The SJ circumscribes the cell, and
855 the PAAC has coalesced with the gut lumen. The pre-enterocyte is still smaller than mature entero-
856 cytes and has a concave, rather than convex apical-luminal surface, but the relative arrangement of
857 its SJ, apical, and basolateral surfaces are topologically equivalent to a mature enterocyte.

858

859

Figure S2

860

861

Figure S2 (related to Figure 3A-C). The A142 splice trap transposon is inserted into CG2556/Meduse, a novel protein that co-localizes with actin filaments.

862

863

864

865

866

867

868

(A) Genomic location of the splice trap transposon in the A142 line. The insertion was mapped by inverse PCR and genomic PCR to the large first intron of CG2556, approximately 10.6 kb downstream of the splice site in Exon 1. The transposon is inserted in the proper orientation to capture transcripts from CG2556, which would result in an N-terminal GFP tag on the nearly undisturbed protein (Exon 1 encodes only 7 amino acids including the initiator Met). The tentacular appearance of the fusion protein in oocytes prompted us to name the gene Meduse (Mdu).

869

(B) Mdu::GFP co-localizes with cortical actin filaments in Stage 10 oocytes.

870

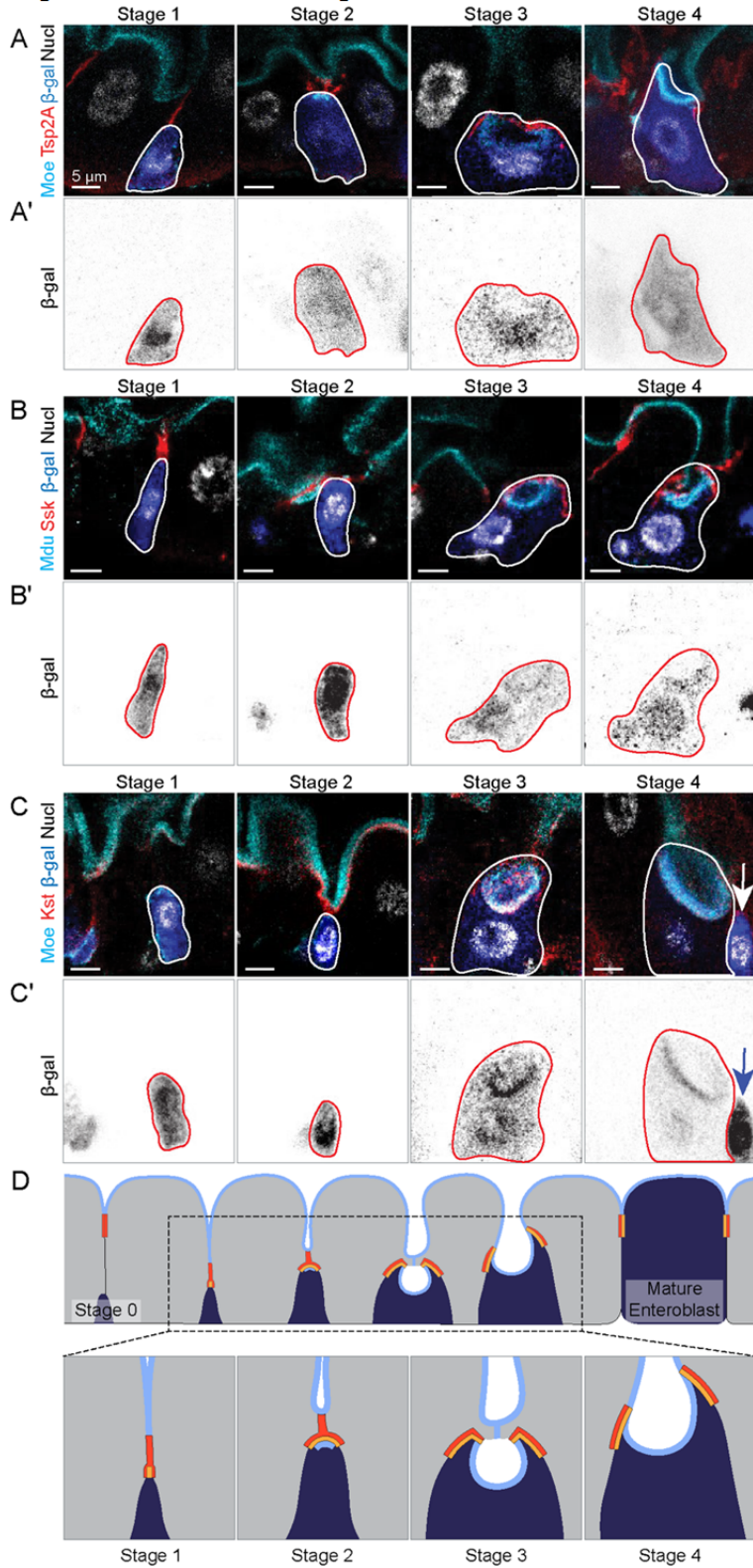
871

872

873

(C) Latrunculin B (LatB) treatment disrupts cortical actin filaments (red, Rhodamin-phalloidin) in the oocyte and leads to abrogation of the oocyte Mdu::GFP signal. Note that LatB does not disrupt actin in ring canals; localization of Mdu::GFP to ring canals is visible in Panels C and C'. Full genotype in Table 1.

874

Figure S3 (related to Figure 3A-C)

876

877 **Figure S3 (related to Figure 3A-C). Immunostaining of *Su(H)*-driven β -galactosidase in**
 878 **integrating cells.**

879 (A-C) The same four-channel images shown in Figure 3 are repeated above the correspond-
 880 ing, single-channel images of β -galactosidase immunostain. The presence of β -galactosidase in Stage

881 3 and Stage 4 cells demonstrates that these cells derived recently from enteroblasts. During acquisi-
882 tion of the Stage 3 and 4 images, the gain was increased compared to Stages 1 and 2 to visualize
883 lower levels of β -galactosidase. Arrowheads in C and C' point to a Stage 1 enteroblast next to the
884 Stage 4 pre-enterocyte; at the higher gain necessary to visualize β -galactosidase in the Stage 4 pre-
885 enterocyte, β -galactosidase intensity in the Stage 1 enteroblast is overexposed. Images are projec-
886 tions of short confocal stacks.

887 (D) Four-stage model of epithelial integration. A newborn enteroblast (Stage 0) forms SJ con-
888 tacts between their apex and the basal edge of enterocyte-enterocyte SJs (Stage 1). The enteroblast-
889 enterocyte SJ broadens, and apical markers accumulate at its cytoplasmic face (Stage 2). The entero-
890 blast grows into a pre-enterocyte, characterized by the expansion of apical markers into a PAAC and
891 broadening of the SJ into a diaphragm-like sheet (Stage 3). The PAAC's lumen fuses with the gut's
892 central lumen, and SJs remodel to circumscribe the cell (Stage 4). Eventually, the concave luminal-
893 apical surface everts to form the convex apical surface that characterizes mature enterocytes. Enter-
894 oblast/pre-enterocyte SJs shown in orange, mature enterocyte SJs in red, and apical surface in light
895 blue. Full genotypes in Table 1.

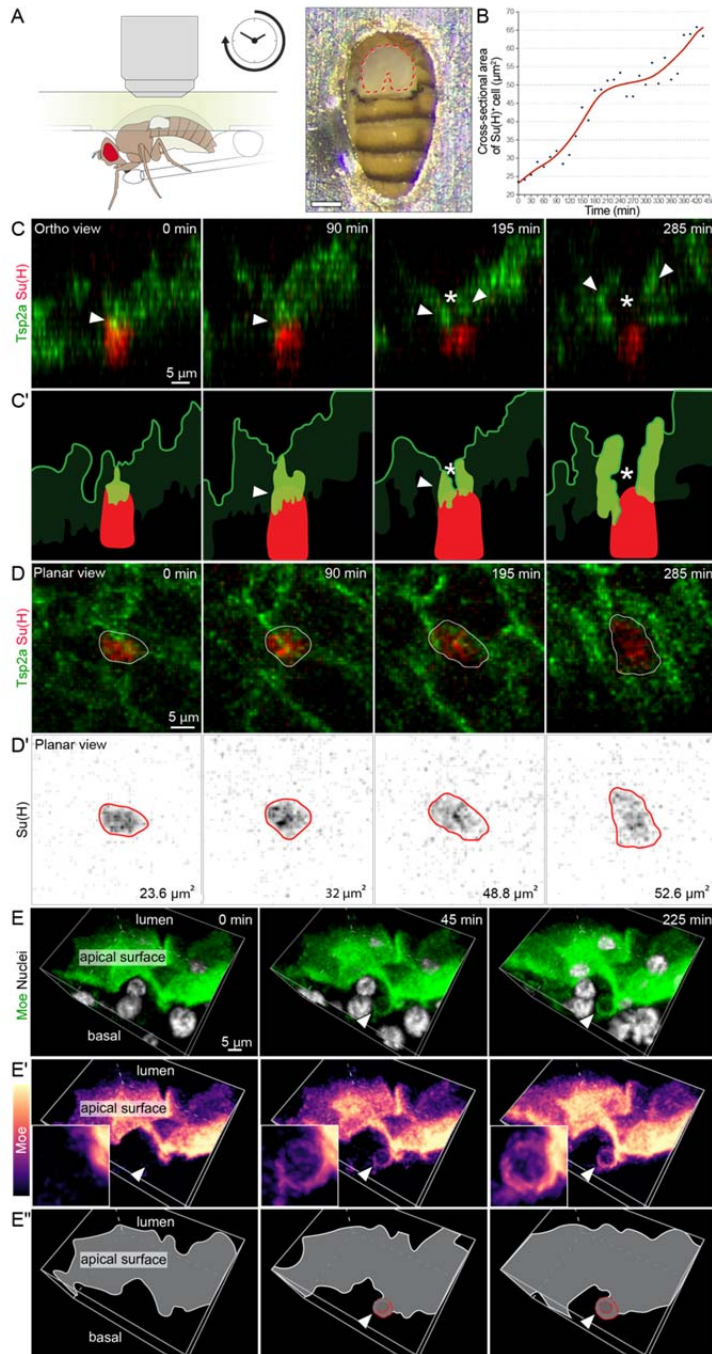
896

897 **Video 3 (related to Figure 3A). 360° confocal reconstruction of a Stage 3 pre-enterocyte**
898 **shows that the PAAC's apical membrane is distinct from the gut's lumenal-apical surface.**

899 Video shows reconstructed 360° view of a Stage 3 pre-enterocyte, labeled by Su(H)-driven
900 β -galactosidase. The pre-enterocyte is surrounded by two mature enterocytes, and a pair of small,
901 basal progenitor cells is visible between the pre-enterocyte and one of the mature enterocytes. The
902 apical marker Moesin::GFP outlines the lumenal-apical surface of the mature enterocytes, the PAAC
903 in the pre-enterocyte, and the entire cortex of the progenitor cells. The SJ protein Tetraspanin2A
904 forms a convex web that covers the apex of the pre-enterocyte. Nuclei are labelled with DAPI. Full
905 genotype in Table 1.

906

Figure 4



908

909 **Figure 4: *In vivo* live imaging of SJ and PAAC dynamics supports the four-stage model of**
 910 **integration.**

911 (A) Continuous time-lapse imaging of midguts in live, feeding *Drosophila* was performed
 912 through a window in the dorsal cuticle. Adapted from Martin, 2018.

913 (B) Cross-sectional area of the *Su(H)-mCherry*⁺ cell shown in Panels C and D and in Video 4.
 914 The increase in area implies that this cell is actively differentiating from enteroblast to enterocyte.

915 (C-D) Live dynamics of SJ during enteroblast-enterocyte differentiation. Still frames are from
 916 a 7.25 h volumetric movie (Video 4) of a midgut expressing *GS5961-tsp2A::GFP* and *Su(H)-mCherry*.

917 The cell analyzed in Panel B is shown in ortho view (C; apical at top) with corresponding line draw-
918 ings (C'). In ortho view, arrowheads point to the SJ associated with this cell and asterisk denotes es-
919 timated location of putative PAAC. The planar view is shown in (D); panels are projections of serial
920 confocal images. Numbers in the lower right corner of panels in D' are cross-sectional areas of the
921 cell at the given time points. SJ morphogenesis over time is visible in the ortho view: Between 0 min
922 and 90 min, the SJ broadens over the cell's apex. At 195 min, a hollow space (asterisk in C) develops
923 along the SJ's apical-basal axis. Between 195 and 225 min, the hollow space widens; both the hollow
924 space and its surrounding SJ elongate along the lateral edges of the now-larger cell.

925 (E) Live imaging of PAAC development. Still frames from a 3.75 h volumetric movie (Video
926 5) of midgut expressing the apical marker *moe::GFP* (green in E; magma LUT in E') and the nuclear
927 marker *ubi-his2av::RFP* (grayscale in E). Corresponding line drawings are in E'. Arrowhead in E'
928 points to the area of PAAC formation, which is also shown as a close-up in the inset. At 0 min, the
929 lumenal-apical surface appears as a lumpy blanket overlying the gut cell nuclei; no PAAC is visible.
930 By 45 min, a putative PAAC has formed at the basal side of the lumenal-apical surface. By 225 min,
931 the PAAC has become deeper and brighter. Insets in E' show close-up views of the developing
932 PAAC. Full genotypes for all panels in Table.

933

934 **Video 4 (related to Figure 4C and 4D). 7.5-hour continuous time-lapse of SJ dynamics**
935 **during enteroblast-enterocyte differentiation.**

936 Windowmount imaging of midgut expressing *GS5961-tsp2A::GFP* and *Su(H)-mCherry*. Planar
937 (top) and ortho (bottom) views of the same tissue volume are shown. In ortho view, the dotted white
938 line indicates the basal surface of the differentiating cell. Arrowhead points to SJs (*Tsp2A::GFP*) as-
939 sociated with the differentiating, *mCherry*⁺ cell analyzed in Fig. 4B. Dynamics of the SJ in ortho view
940 are consistent with the four-stage mechanism inferred from Fig. 3: Nascent contact (Stage 1), broad-
941 ening and expansion over the cell apex (Stages 2-3), and central hollowing and lateral extension
942 (Stage 4). Full genotype in Table 1.

943

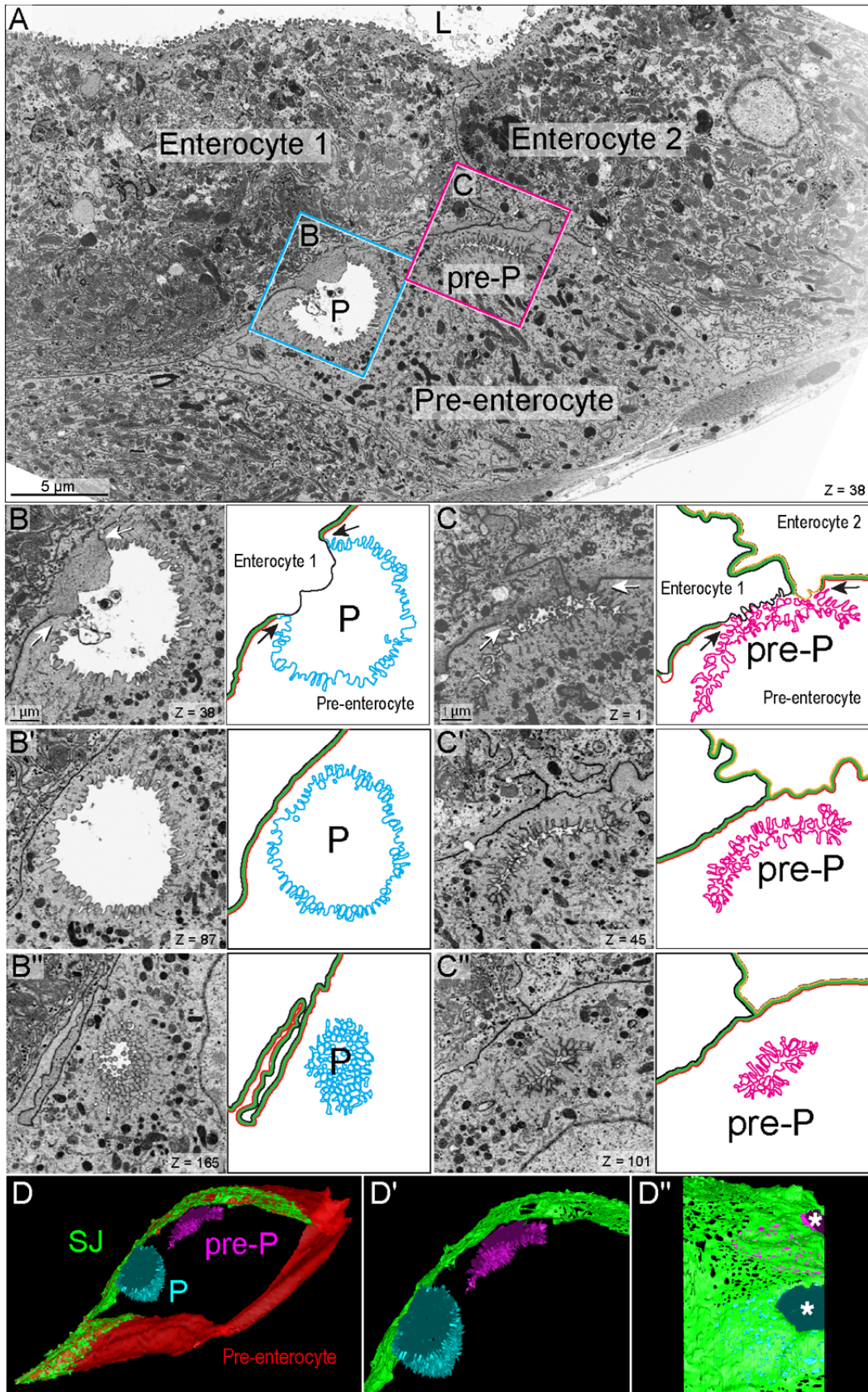
944 **Video 5 (related to Figure 4E). 3.75-hour continuous time-lapse movie of PAAC develop-**
945 **ment.**

946 Windowmount imaging of midgut expressing *moesin::GFP* and *ubi-his2av::RFP*. The
947 *Moesin::GFP* channel (magma LUT) is shown without (left) and with (right) the *His2av::RFP* channel
948 (grayscale). At 30 min, a faint *Moesin::GFP*-labelled structure (arrowhead) forms at the basal side of
949 the gut's lumenal-apical surface. The concave shape of this structure is similar to PAACs in fixed
950 samples (Fig. 3, Stage 3; Video 3). From 30-225 min, the putative PAAC deepens, and its GFP-
951 labelled boundary brightens and thickens. Full genotype in Table 1.

952

953
954

Figure 5



955

956 **Figure 5. PAACs are intercellular lumens with split apical-basolateral polarity.**

957 (A) One slice of a representative, 200-slice FIB-SEM tomographic series. Series captures two
958 mature enterocytes that contact the gut's central lumen (L) and an underlying pre-enterocyte, which
959 does not. An ellipsoid-shaped PAAC (P, cyan box) and an allantoid-shaped PAAC precursor (pre-P,
960 magenta box) appear at the apex of the pre-enterocyte. See Figure S4.

961 (B) Close-up of the PAAC in cyan box in A. Three FIB-SEM sections are shown next to car-
962 toon representations. P indicates the PAAC lumen. In cartoons, the apical membrane of the pre-
963 enterocyte is cyan, the basolateral membrane of the pre-enterocyte is red, the basolateral plasma
964 membrane of enterocyte 1 is black, and the SJ between the pre-enterocyte and enterocyte 1 is green.
965 In B, a gap in the SJ reveals that the PAAC is an intercellular lumen between the apical pre-
966 enterocyte membrane and the basolateral enterocyte membrane (split polarity). Arrows point to the
967 three-way boundary between the pre-enterocyte apical membrane, the enterocyte basolateral mem-
968 brane, and the pre-enterocyte basolateral membrane. In B' and B'', the deep cytoplasmic invagination
969 of the pre-enterocyte apical membrane forms most of the PAAC's luminal volume.

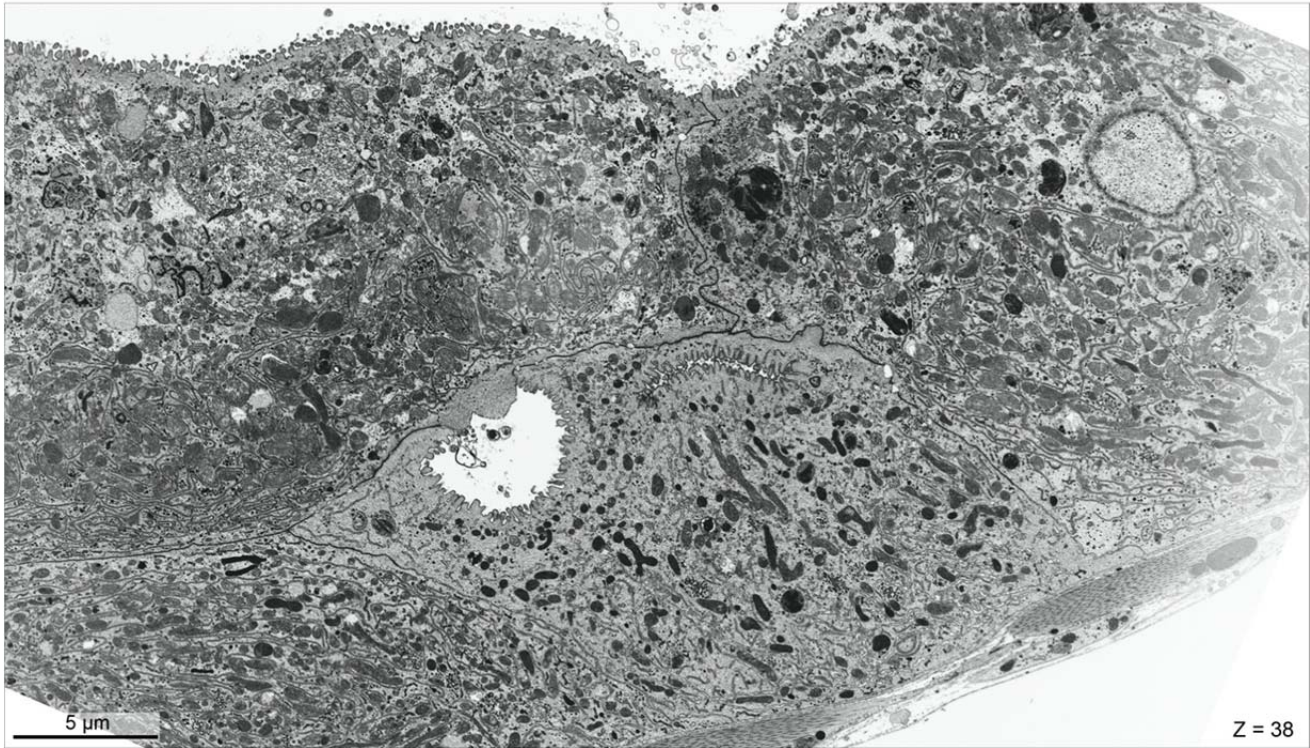
970 (C) Close-up of the PAAC precursor in magenta box in A. pre-P indicates the PAAC precur-
971 sor. In cartoons, the pre-enterocyte's apical membrane is magenta, the pre-enterocyte's basolateral
972 membrane is red, the basolateral plasma membrane of enterocyte 1 is black, the basolateral mem-
973 brane of enterocyte 2 is orange, and the SJ between the pre-enterocyte and enterocytes 1 and 2 is
974 green. In C, a gap in the SJ reveals that the PAAC precursor is an intercellular lumen. Arrows point
975 to two three-way boundaries between the pre-enterocyte apical membrane, the basolateral mem-
976 brane of either enterocyte 1 or enterocyte 2, and the pre-enterocyte basolateral membrane. In C' and
977 C'', the precursor's slender, allantoid-shaped lumen arises through invagination of the pre-
978 enterocyte's convoluted apical membrane. In A-C, Z values in lower left of panels are slice numbers.

979 (D) Volumetric rendering of 200 FIB-SEM sections, including the section in A. Apical mem-
980 branes of the pre-enterocyte are cyan (PAAC) and magenta (PAAC precursor), basolateral mem-
981 brane of the pre-enterocyte is red, and SJ between the pre-enterocyte and mature enterocytes is in
982 green. Zoomed-in panels show the PAAC, PAAC precursor, and SJ in a cutaway view (D') and a
983 top-down view (D''). In D and D', the PAAC's ellipsoid shape and the precursor's allantoid shape
984 are evident. In D'', asterisks mark holes in the SJ resulting from separation of pre-enterocyte and en-
985 terocyte plasma membranes during PAAC formation. (Enterocyte membranes not shown.) See Vid-
986 eo 6. Full genotype in Table 1.

987

988

Figure S4 (related to Figure 5A)



989

990 **Figure S4 (related to Figure 5A). High resolution view of FIB-SEM section shown in Fig-**
991 **ure 4A.**

992 40nm-thick sections were cut with a gallium ion beam at 2kV, 0.8 nA, 4.2mm working dis-
993 tance, 5μs dwell time, 6144x4096 frame size. Pixel size 9.7nm. Full genotype in Table 1.

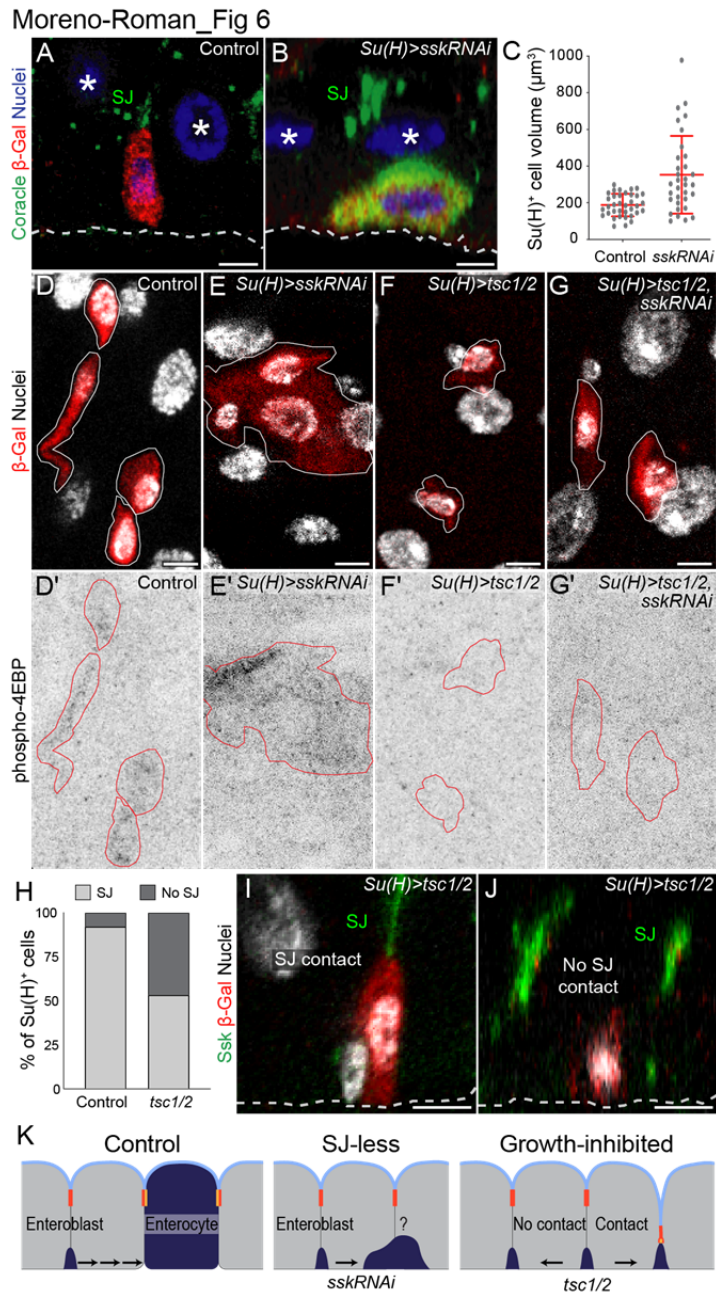
994

995 **Video 6 (related to Figure 5A-D). Three-dimensional ultrastructure of PAAC, PAAC pre-**
996 **cursor, and their associated pre-enterocyte.**

997 Tomographic reconstruction of 200 serial FIB-SEM images, including a cropped version of
998 the image shown in Figures 5A and S4. 360° rotation reveals the ellipsoid and allantoid shapes of the
999 PAAC and PAAC precursor, respectively, and also reveals holes in the SJ in which the pre-
1000 enterocyte and enterocyte membranes have separated to form the intercellular lumens. Volume of
1001 reconstruction: 40.2 μm x 23.9 μm x 8 μm. Slice thickness, 40 nm. Full genotype in Table 1.

1002

1003



1005

1006

Figure 6. Cells must form SJs and grow in order to integrate.

1007

1008

1009

1010

1011

1012

(A-C) Blocking SJ formation prevents integration but not growth. (A) Cross-sectional view of control *Su(H)*⁺ cell (red, *Su(H)-lacZ*). The cell's apex has formed contacts with the basal tip of the SJ (green, Coracle) between neighbor enterocytes. (B) Cross-sectional view of *Su(H)^{ts}>sskRNAi*. The cell expresses *Su(H)-lacZ* (red) and high levels of Coracle (green), which localizes to the cytoplasm. It does not contact either enterocyte-enterocyte SJs or the gut lumen. (C) Measurements of cytoplasmic volumes show that *Su(H)^{ts}>sskRNAi* cells become larger in size compared to control *Su(H)* cells.

1013

1014

(D-G) Growth of *Su(H)^{ts}>sskRNAi* cells requires Tor pathway activation. Planar views of all midgut cell nuclei (grayscale, DAPI) and *Su(H)-lacZ* (red) are shown above corresponding images of

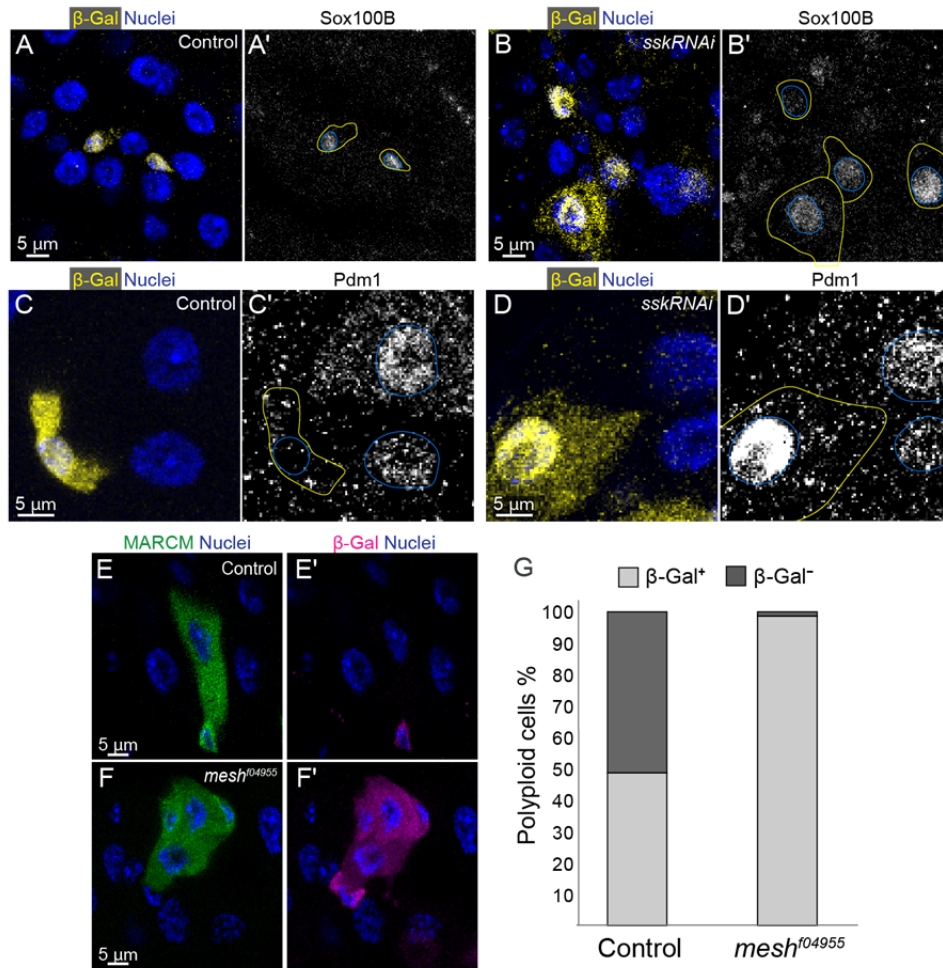
1015 phospho-4EBP immunostain (D'-G', inverted grayscale). *Su(H)-lacZ*-labelled cells are outlined in
1016 white (D-G) and red (D'-G'). Control *Su(H)* cells (D) and *Su(H)^{ts}>sskRNAi* (E) cells are phospho-
1017 4EBP⁺ (D', E'). Tor-inhibited, *Su(H)^{ts}>tsc1/2* (F) and *Su(H)^{ts}>sskRNAi, tsc1/2* (G) are not (F', G').

1018 (H-J) Growth-inhibited enteroblasts arrest at initial stages of integration. The frequency with
1019 which *Su(H)^{ts}>tsc1/2* cells (*Su(H)-lacZ*, red) contact the gut SJ network (Ssk, green) is reduced to 53%
1020 from the control frequency of 92% (H). Both *Su(H)^{ts}>tsc1/2* cells that contact SJs (I) and those that do
1021 not (J) fail to reach the gut's luminal surface. N=3 control midguts (214 enteroblasts) and 3
1022 *Su(H)>tsc1/2* midguts (146 enteroblasts). All scale bars, 5 μ m. Full genotypes in Table 1.

1023 (K) Cartoon summary: (Left) Control. Integration requires both cell growth and SJ formation.
1024 (Middle) Blocking SJ formation prevents integration but does not halt growth. (Right) Growth inhi-
1025 bition arrests cells in Stages 0-1 of integration.

1026

Figure S5



1028

1029 **Figure S5 (Related to Figure 6). SJ-less cells exhibit an abnormal mix of enteroblast and**
 1030 **enterocyte features.**

1031 (A-B) *Su(H)*^{ts}>*sskRNAi* cells express the stem cell/enteroblast transcription factor Sox100B.
 1032 Planar views of control *Su(H)* cells (A) and *Su(H)*^{ts}>*sskRNAi* cells. (B). Left panels: Yellow, *Su(H)*-*lacZ*
 1033 (β -gal immunostain); blue, nuclei (DAPI). Right panels: Sox100B immunostain. Yellow and blue out-
 1034 lines in right panels indicate *Su(H)*-*lacZ*⁺ cells and their nuclei, respectively.

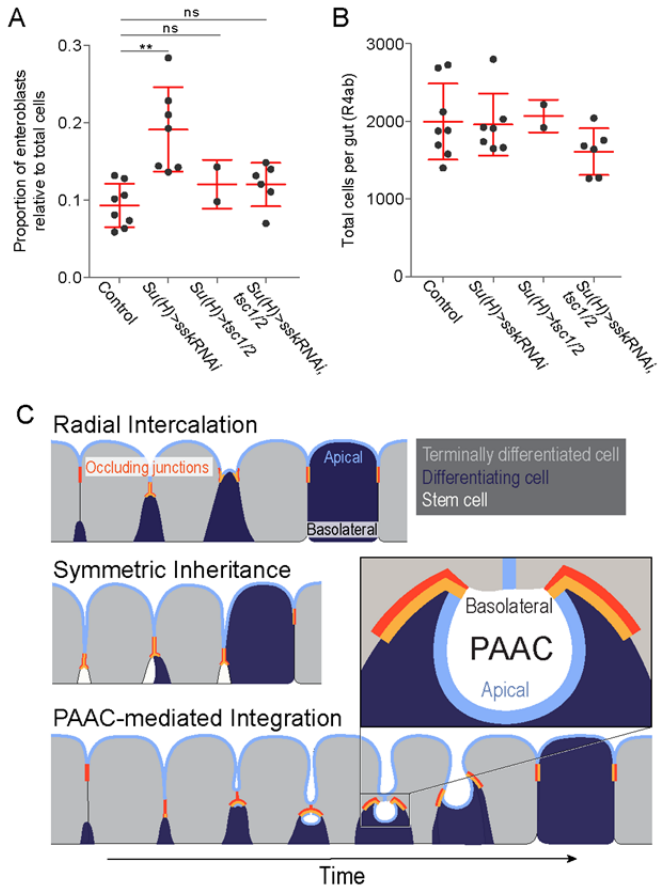
1035 (C-D) *Su(H)*^{ts}>*sskRNAi* cells express the enterocyte-specific transcription factor Pdm1. Con-
 1036 trol *Su(H)* cells (C) and *Su(H)*^{ts}>*sskRNAi* cells are shown. Left panels: Yellow, *Su(H)*-*lacZ* (β -gal im-
 1037 munostain); blue, nuclei (DAPI). Right panels: Pdm1 immunostain. Yellow and blue outlines in right
 1038 panels indicate *Su(H)*-*lacZ*⁺ cells and their nuclei, respectively.

1039 (E-G) *Su(H)*-*lacZ* expression in stem cell (MARCM) clones that are either control (E) or *mesh*-
 1040 null (*mesh*^{f04955}) (E). 4-day clones are labelled with GFP (green). β -gal immunostain (red) identifies
 1041 *Su(H)*-*lacZ*-expressing cells. Nuclei are stained with DAPI (blue). In control clones, 52% of polyploid
 1042 cells have lost β -Gal staining (n=39 polyploid cells from 133 clones, N=3 midguts), implying that
 1043 terminal differentiation of polyploid cells to enterocyte fate is complete. In *mesh*-null clones, only 1.1%
 1044 of cells has lost β -gal staining, implying that nearly all cells, despite being polyploid, have not com-

1045 pleted terminal differentiation (n=89 polyploid cells from 149 clones, N=3 midguts). All scale bars, 5
1046 μm . Full genotypes in Table 1.

1047

Figure 7



1049

Figure 7. Impact of blocked midgut cell integration on organ-scale cell equilibrium.

1051 (A) Proportion of $Su(H)^+$ cells in midguts with blocked cell integration. Plots show the per-
 1052 centage of $Su(H)$ - $lacZ^+$ cells relative to total cells in the R4ab region of midguts with the indicated
 1053 genotypes. Cell integration was blocked by inhibiting either new SJ formation ($Su(H)^{ts}>sskRNAi$),
 1054 cell growth ($Su(H)^{ts}>tsc1/2$), or both ($Su(H)^{ts}>sskRNAi, tsc1/2$) between days 4-8 of adult life. Each
 1055 data point represents one midgut. Red lines show Means \pm S.D for each condition: $Su(H)$ control -
 1056 0.09 ± 0.03 cells; $Su(H)^{ts}>sskRNAi$ - 0.19 ± 0.05 ; $Su(H)^{ts}>tsc1/2$ - 0.12 ± 0.032 cells; $Su(H)^{ts}>sskRNAi,$
 1057 $tsc1/2$ - 0.12 ± 0.028 cells.

1058 (B) Total numbers of midgut cells remain constant when cell integration is blocked. Plots
 1059 show total counts of DAPI-labeled nuclei in the R4ab regions of midguts analyzed in Panel A. Each
 1060 data point represents one midgut. Red lines show Means \pm S.D for each condition: $Su(H)$ control -
 1061 1997 ± 489 cells; $Su(H)^{ts}>sskRNAi$ - 1960 ± 398 ; $Su(H)^{ts}>tsc1/2$ - 2067 ± 210 cells; $Su(H)^{ts}>sskRNAi,$
 1062 $tsc1/2$ - 1611 ± 299 cells.

1063 (C) Three mechanisms to incorporate stem cell progeny into a mature epithelium. Only
 1064 PAAC-mediated integration enables the differentiating cell to form new barrier structures (apical
 1065 plasma membrane and occluding junctions) while still sheltered by the mature occluding junction
 1066 barrier.

1067

TABLE 1 – Genotypes in Figure Panels

FIGURE	GENOTYPE
Fig 1 A	<i>MduA142GFP/ Su(H)-lacZ</i> (X Chr)
Fig 1 B-H	<i>esg-Gal4, UAS-His2b::CFP; Su(H)-GFP::nls</i>
Fig 2	<i>esg-Gal4, UAS-His2b::CFP; Su(H)-GFP::nls, ubiP-His2av::mRFP</i>
Fig 3 A	<i>Su(H)-lacZ/ +; +; ubiP-His2AV::mRFP, Sqh-Moesin::GFP/ +</i>
Fig 3 B	<i>MduA142GFP/ Su(H)-lacZ</i> (X Chr) <i>MduA142GFP/ +; Su(H)-Gal4/ +; Su(H)-lacZ, tubP-Gal80ts/ +</i>
Fig 3 C	<i>Su(H)-lacZ/ +; +; ubiP-His2AV::mRFP, Sqh-Moesin::GFP/ +</i>
Fig 4 B-D	<i>UAS-Tsp2aGFP/ +; Su(H)-mCherry/ 5966GS-Gal4; +</i>
Fig 4 E	<i>ubiP-His2Av::mRFP, sqhP-Moe::GFP</i>
Fig 5	<i>esg-Gal4, UAS-His2b::CFP; Su(H)-GFP::nls, ubiP-His2av::mRFP</i>
Fig 6 A	<i>Su(H)-Gal4, UAS-mCD8::GFP/ +; Su(H)-lacZ, tubP-Gal80ts/ +</i>
Fig 6 B	<i>Su(H)-Gal4, UAS-mCD8::GFP/ UAS-sskRNAi; Su(H)-lacZ, tubP-Gal80ts/ +</i>
Fig 6 C	Same as Fig 6 A&B
Fig 6 D	<i>Su(H)-Gal4, UAS-mCD8::GFP/ +; Su(H)-lacZ, tubP-Gal80ts/ +</i>
Fig 6 E	<i>Su(H)-Gal4, UAS-mCD8::GFP/ UAS-sskRNAi; Su(H)-lacZ, tubP-Gal80ts/ +</i>
Fig 6 F	<i>Su(H)-Gal4, UAS-mCD8::GFP/ +; Su(H)-lacZ, tubP-Gal80ts/ UAS-Tsc1/2</i>
Fig 6 G	<i>Su(H)-Gal4, UAS-mCD8::GFP/ UAS-sskRNAi; Su(H)-lacZ, tubP-Gal80ts/ UAS-Tsc1/2</i>
Fig 6 H	Ctrl: <i>esg-Gal4, UAS-His2b::CFP; Su(H)-GFP::nls</i> Su(H)> tsc1/2: <i>Su(H)-Gal4, UAS-mCD8::GFP/ +; Su(H)-lacZ, tubP-Gal80ts/ UAS-Tsc1/2</i>
Fig 6 I	<i>Su(H)-Gal4, UAS-mCD8::GFP/ +; Su(H)-lacZ, tubP-Gal80ts/ UAS-Tsc1/2</i>
Fig 6 J	<i>Su(H)-Gal4, UAS-mCD8::GFP/ +; Su(H)-lacZ, tubP-Gal80ts/ UAS-Tsc1/2</i>
Fig 7 A	Ctrl: <i>Su(H)-Gal4, UAS-mCD8::GFP/ +; Su(H)-lacZ, tubP-Gal80ts/ +</i> Su(H)> sskRNAi: <i>Su(H)-Gal4, UAS-mCD8::GFP/ UAS-sskRNAi; Su(H)-lacZ, tubP-Gal80ts/ +</i> Su(H)> tsc1/2: <i>Su(H)-Gal4, UAS-mCD8::GFP/ +; Su(H)-lacZ, tubP-Gal80ts/ UAS-Tsc1/2</i> Su(H)> tsc1/2, sskRNAi: <i>Su(H)-Gal4, UAS-sskRNAi/ +; Su(H)-lacZ, tubP-Gal80ts/ UAS-Tsc1/2</i>
Fig 7 B	Same as Fig 7 A
Fig 7 C	Same as Fig 7 A
Fig S1	<i>esg-Gal4, UAS-His2b::CFP; Su(H)-GFP::nls, ubiP-His2av::mRFP</i>
Fig S2 B&C	<i>MduA142GFP</i> (X Chr)
Fig S3	<i>Su(H)-lacZ/ +; +; ubiP-His2AV::mRFP, Sqh-Moe::GFP/ +</i>
Fig S4	<i>esg-Gal4, UAS-His2b::CFP; Su(H)-GFP::nls, ubiP-His2av::mRFP</i>
Fig S5 A	<i>Su(H)-Gal4, UAS-mCD8::GFP/ +; Su(H)-lacZ, tubP-Gal80ts/ +</i>
Fig S5 B	<i>Su(H)-Gal4, UAS-mCD8::GFP/ UAS-sskRNAi; Su(H)-lacZ, tubP-Gal80ts/ +</i>
Fig S5 C	<i>Su(H)-Gal4, UAS-mCD8::GFP/ +; Su(H)-lacZ, tubP-Gal80ts/ +</i>
Fig S5 D	<i>Su(H)-Gal4, UAS-mCD8::GFP/ UAS-sskRNAi; Su(H)-lacZ, tubP-Gal80ts/ +</i>
Fig S5 E	<i>w, UAS-mCD8::GFP, hsf1p¹²²/ Su(H)-lacZ; tubP-Gal4/ +; FRT82B/ FRT82B, tubP-Gal80</i>
Fig S5 F	<i>w, UAS-mCD8::GFP, hsf1p¹²²/ Su(H)-lacZ; tubP-Gal4/ +; mesh¹⁰⁴⁹⁵⁵/ FRT82B, tubP-Gal80</i>
Fig S5 G	Same as Fig S5 E&F

TABLE 2 – Reagents and Resources

REAGENT or RESOURCE	SOURCE	IDENTIFIER
Antibodies		
Mouse anti-Armadillo	DSHB	N2 7A1; RRID: AB_528089
Mouse anti-Coracle	DSHB	C615.16; RRID: AB_1161644
Mouse anti- β -galactosidase	Promega	Z3781; RRID: AB_430877
Donkey anti-mouse Alexa Fluor 647	Invitrogen	A-31571; RRID: AB_162542
Donkey anti-rabbit Alexa Fluor 555	Invitrogen	A-31572; RRID: AB_162543
Goat anti-Chicken Alexa Fluor 488	Invitrogen	A-11039; RRID: AB_2534096
Goat anti-Rabbit Alexa Fluor 405	Thermo Fisher	RRID: AB_221605
GFP Polyclonal Antibody, Alexa Fluor 488	Thermo Fisher	A-21311; RRID: AB_221477
Goat anti-Mouse Alexa Fluor 405	Thermo Fisher	A-31553; RRID: AB_221604
Goat anti-Mouse Alexa Fluor 647	Thermo Fisher	A-21240; RRID: AB_2535809
Goat anti-Mouse Alexa Fluor 555	Thermo Fisher	A-21137; RRID: AB_2535776
Goat anti-Rabbit Alexa Fluor 647	Thermo Fisher	A-21244; RRID: AB_2535812
Rabbit anti-Phospho4EBP1	Cell Signaling Technology	RRID: AB_560835
Rabbit anti-Pdm1	Yang lab	N/A
Rabbit anti-Snakeskin	Furuse lab	N/A
Rabbit anti-Tetraspanin2A	Furuse lab	N/A
Rabbit anti-Sox100B	Russell lab	N/A
Rabbit anti-Karst	Thomas lab	N/A
Chemicals, Peptides, and Recombinant Proteins		
Rhodamine Phalloidin	Invitrogen	R415; CAS Number 219920-04-4
RU486	Sigma-Aldrich	M8046-100MG; CAS Number 84371-65-3
DAPI	Thermo Fisher	RRID: AB_2629482
Prolong Gold antifade	Thermo Fisher	P10144
Isradipine	Millipore Sigma	I6658; CAS Number 75695-93-1
Experimental Models: Organisms/Strains		
<i>Drosophila: mesh¹⁰⁴⁹⁵⁵</i>	BDSC	18826; FLYB: FBti0042412
<i>Drosophila: SqhP-Moesin::GFP</i>	BDSC	59023; FLYB: FBti0016051
<i>Drosophila: Su(H)-Gal4</i>	BDSC	93377; FLYB: FBti0204714
<i>Drosophila: ubiP-His2av::mRFP</i>	BDSC	FLYB: FBti0077846; RRID: BDSC 23650
<i>Drosophila: Su(H)-lacZ (3rd Chr)</i>	BDSC	83352; FLYB: FBtp0014034
<i>Drosophila: tubP-Gal80ts</i>	BDSC	7017; FLYB: FBti0027797
<i>Drosophila: UAS-SskRNAi</i>	VDRC	105193; PMID: 22328496
<i>Drosophila: esg-Gal4</i>	Kyoto DGGR	112304; FLYB: FBti0033872
<i>Drosophila: UAS-His2b::CFP</i>	Yoshihiro Inoue lab	PMID: 24850412
<i>Drosophila: FRT82B</i>	David Bilder lab	FLYB: FBti0002074
<i>Drosophila: UAS-mCD8GFP</i>	David Bilder lab	FLYB: FBtp0002652
<i>Drosophila: 5966GS-Gal4</i>	Henri Jasper lab	FLYB: FBti0150384
<i>Drosophila: UAS-Tsc1/2</i>	Nicolas Tapon lab	PMID: 20573703
<i>Drosophila: Su(H)-mCherry</i>	Allison Bardin lab	N/A
<i>Drosophila: Su(H)-lacZ (X Chr)</i>	Sarah Siegrist lab	N/A
<i>Drosophila: MduA142GFP</i>	Nicolas Buchon lab	N/A
<i>Drosophila: UAS-Tsp2aGFP</i>	Norbert Perrimon lab	N/A
<i>Drosophila: Su(H)-GFP::nls</i>	Joaquin de Navascués lab	PMID: 22522699

(Continued on next page)

Continued

REAGENT or RESOURCE	SOURCE	IDENTIFIER
Oligonucleotides		
<i>traF</i> _U primer: CGAGAAAGAGAATAC-CATGGGCGATCAA	N/A	N/A
<i>traF</i> _L primer: CCTGTGGTGGCACTTGCACATAGTA	N/A	N/A
<i>GFP</i> _62U primer: CGACGTAAAC-GGCCACAAGTTCA	N/A	N/A
<i>GFP</i> _495L primer: CCTCGATGTTGTGGCG-GATCTTGAA	N/A	N/A
3'Pout_U primer: CATATCGCTGTCTCAC-TCAGACTCAA	N/A	N/A
<i>Mdu3</i> 'conf_L2 primer: CGCGCCACTATGTGCCGCAAA	N/A	N/A
<i>Mdu3</i> 'conf_L1 primer: GCCAAAAGGCATAAAAACAGCTAA	N/A	N/A
<i>Mdu5</i> 'conf_U1 primer: GTGTCAATGGCCCAGAGACCA	N/A	N/A
<i>Mdu5</i> 'conf_U2 primer: GAAATGGGTATGAACTGCAAATCAGTA	N/A	N/A
<i>Mdu5</i> 'conf_U3 primer: GAACAGGCAACAGATGCCAGATAATACA	N/A	N/A
5'Pout_L1 primer: CTTCGGTAAGCTTCGGCTATCGA	N/A	N/A
5'Pout_L2 primer: CTCAACAAGCAAACGTGCACTGAA	N/A	N/A
Software and Algorithms		
Fiji	https://fiji.sc	RRID:SCR_002285
Bitplane Imaris 8	Bitplane	RRID:SCR_007370
IMOD	https://bio3d.colorado.edu/imod/	RRID:SCR_003297
Graphpad Prism 7	GraphPad Software	RRID:SCR_002798

1073

1074 REFERENCES

- 1075 Akagi, K., Wilson, K.A., Katewa, S.D., Ortega, M., Simons, J., Hilsabeck, T.A., Kapuria, S., Sharma,
1076 A., Jasper, H., and Kapahi, P. (2018). Dietary restriction improves intestinal cellular fitness to en-
1077 hance gut barrier function and lifespan in *D. melanogaster*. *PLOS Genetics* *14*, e1007777.
- 1078 Alvers, A.L., Ryan, S., Scherz, P.J., Huiskens, J., and Bagnat, M. (2014). Single continuous lumen
1079 formation in the zebrafish gut is mediated by smoothed-dependent tissue remodeling. *Development*
1080 *141*, 1110–1119.
- 1081 Amcheslavsky, A., Ito, N., Jiang, J., and Ip, Y.T. (2011). Tuberosclerosis complex and Myc coor-
1082 dinate the growth and division of *Drosophila* intestinal stem cells. *The Journal of Cell Biology* *193*,
1083 695–710.
- 1084 Arganda-Carreras, I., Sorzano, C.O.S., Marabini, R., Carazo, J.M., Ortiz-de-Solorzano, C., and Kybic,
1085 J. (2006). Consistent and elastic registration of histological sections using vector-spline regularization.
1086 In *Computer Vision Approaches to Medical Image Analysis*, (Berlin, Heidelberg: Springer, Berlin,
1087 Heidelberg), pp. 85–95.
- 1088 Bachmair, A., Finley, D., and Varshavsky, A. (1986). In vivo half-life of a protein is a function of its
1089 amino-terminal residue. *Science* *234*, 179–186.

- 1090 Bagnat, M., Cheung, I.D., Mostov, K.E., and Stainier, D.Y.R. (2007). Genetic control of single lumen
1091 formation in the zebrafish gut. *Nature Cell Biology* 9, 954–960.
- 1092 Bardin, A.J., Perdigoto, C.N., Southall, T.D., Brand, A.H., and Schweisguth, F. (2010). Transcrip-
1093 tional control of stem cell maintenance in the *Drosophila* intestine. *Development* 137, 705–714.
- 1094 Baumann, O. (2001). Posterior midgut epithelial cells differ in their organization of the membrane
1095 skeleton from other *drosophila* epithelia. *Exp Cell Res* 270, 176–187.
- 1096 Blasky, A.J., Mangan, A., and Prekeris, R. (2015). Polarized Protein Transport and Lumen Formation
1097 During Epithelial Tissue Morphogenesis. *Annu. Rev. Cell Dev. Biol.* 31, 575–591.
- 1098 Bobinnec, Y., Marcaillou, C., Morin, X., and Debec, A. (2003). Dynamics of the endoplasmic reticu-
1099 lum during early development of *Drosophila melanogaster*. *Cell Motility* 54, 217–225.
- 1100 Bonfini, A., Dobson, A.J., Duneau, D., Revah, J., Liu, X., Houtz, P., and Buchon, N. (2021). Mul-
1101 tiscala analysis reveals that diet-dependent midgut plasticity emerges from alterations in both stem
1102 cell niche coupling and enterocyte size. *ELife* 10, e64125.
- 1103 Bryant, D.M., Datta, A., Rodríguez-Fraticelli, A.E., Peränen, J., Martín-Belmonte, F., and Mostov,
1104 K.E. (2010). A molecular network for de novo generation of the apical surface and lumen. *Nat Cell*
1105 *Biol* 12, 1035–1045.
- 1106 Buchon, N., Osman, D., David, F.P.A., Yu Fang, H., Boquete, J.-P., Deplancke, B., and Lemaitre, B.
1107 (2013). Morphological and molecular characterization of adult midgut compartmentalization in *Dro-*
1108 *sophila*. *Cell Rep* 3, 1725–1738.
- 1109 Burel, A., Lavault, M.-T., Chevalier, C., Gnaegi, H., Prigent, S., Mucciolo, A., Dutertre, S., Humbel,
1110 B.M., Guillaudeux, T., and Kolotuev, I. (2018). A targeted 3D EM and correlative microscopy meth-
1111 od using SEM array tomography. *Development* 145.
- 1112 Campbell, K., Casanova, J., and Skaer, H. (2010). Mesenchymal-to-epithelial transition of intercalat-
1113 ing cells in *Drosophila* renal tubules depends on polarity cues from epithelial neighbours. *Mech Dev*
1114 127, 345–357.
- 1115 Chan, C.J., Costanzo, M., Ruiz-Herrero, T., Mönke, G., Petrie, R.J., Bergert, M., Diz-Muñoz, A.,
1116 Mahadevan, L., and Hiiragi, T. (2019). Hydraulic control of mammalian embryo size and cell fate.
1117 *Nature* 571, 112–116.
- 1118 Chen, J., Sayadian, A.-C., Lowe, N., Lovegrove, H.E., and St Johnston, D. (2018). An alternative
1119 mode of epithelial polarity in the *Drosophila* midgut. *PLoS Biology* 16, e3000041.
- 1120 Chepko, G., and Dickson, R.B. (2003). Ultrastructure of the putative stem cell niche in rat mammary
1121 epithelium. *Tissue and Cell* 35, 83–93.
- 1122 Chepko, G., and Smith, G.H. (1997). Three division-competent, structurally-distinct cell populations
1123 contribute to murine mammary epithelial renewal. *Tissue and Cell* 29, 239–253.
- 1124 Choi, N.-H., Lucchetta, E., and Ohlstein, B. (2011). Nonautonomous regulation of *Drosophila* midgut
1125 stem cell proliferation by the insulin-signaling pathway. *Proceedings of the National Academy of*
1126 *Sciences* 108, 18702–18707.

- 1127 Cotsarelis, G., Cheng, S.-Z., Dong, G., Sun, T.-T., and Lavker, R.M. (1989). Existence of slow-
1128 cycling limbal epithelial basal cells that can be preferentially stimulated to proliferate: Implications
1129 on epithelial stem cells. *Cell* 57, 201–209.
- 1130 Daniel, E., Daudé, M., Kolotuev, I., Charish, K., Auld, V., and Le Borgne, R. (2018). Coordination of
1131 Septate Junctions Assembly and Completion of Cytokinesis in Proliferative Epithelial Tissues. *Curr.*
1132 *Biol.* 28, 1380-1391.e4.
- 1133 Dantoft, W., Davis, M.M., Lindvall, J.M., Tang, X., Uvell, H., Junell, A., Beskow, A., and Engström,
1134 Y. (2013). The Oct1 homolog Nubbin is a repressor of NF-κB-dependent immune gene expression
1135 that increases the tolerance to gut microbiota. *BMC Biology* 11, 99.
- 1136 Dasgupta, S., Gupta, K., Zhang, Y., Viasnoff, V., and Prost, J. (2018). Physics of lumen growth.
1137 *PNAS* 115, E4751–E4757.
- 1138 Datta, A., Bryant, D.M., and Mostov, K.E. (2011). Molecular Regulation of Lumen Morphogenesis.
1139 *Current Biology* 21, R126–R136.
- 1140 Deblandre, G.A., Wettstein, D.A., Koyano-Nakagawa, N., and Kintner, C. (1999). A two-step mech-
1141 anism generates the spacing pattern of the ciliated cells in the skin of *Xenopus* embryos. *Develop-*
1142 *ment* 126, 4715–4728.
- 1143 DeMaio, L., Tseng, W., Balverde, Z., Alvarez, J.R., Kim, K.-J., Kelley, D.G., Senior, R.M., Crandall,
1144 E.D., and Borok, Z. (2009). Characterization of mouse alveolar epithelial cell monolayers. *American*
1145 *Journal of Physiology-Lung Cellular and Molecular Physiology* 296, L1051–L1058.
- 1146 Dietzl, G., Chen, D., Schnorrer, F., Su, K.-C., Barinova, Y., Fellner, M., Gasser, B., Kinsey, K., Op-
1147 pel, S., Scheiblaue, S., et al. (2007). A genome-wide transgenic RNAi library for conditional gene
1148 inactivation in *Drosophila*. *Nature* 448, 151–156.
- 1149 Doupé, D.P., Marshall, O.J., Dayton, H., Brand, A.H., and Perrimon, N. (2018). *Drosophila* intestinal
1150 stem and progenitor cells are major sources and regulators of homeostatic niche signals. *PNAS* 115,
1151 12218–12223.
- 1152 Dumortier, J.G., Verge-Serandour, M.L., Tortorelli, A.F., Mielke, A., Plater, L. de, Turlier, H., and
1153 Maître, J.-L. (2019). Hydraulic fracturing and active coarsening position the lumen of the mouse
1154 blastocyst. *Science* 365, 465–468.
- 1155 Edwards, K.A., Demsky, M., Montague, R.A., Weymouth, N., and Kiehart, D.P. (1997). GFP-
1156 Moesin Illuminates Actin Cytoskeleton Dynamics in Living Tissue and Demonstrates Cell Shape
1157 Changes during Morphogenesis in *Drosophila*. *Developmental Biology* 191, 103–117.
- 1158 Evans, M.J., and Moller, P.C. (1991). Biology of Airway Basal Cells. *Experimental Lung Research*
1159 17, 513–531.
- 1160 Fleming, E.S., Zajac, M., Moschenross, D.M., Montrose, D.C., Rosenberg, D.W., Cowan, A.E., and
1161 Tirnauer, J.S. (2007). Planar spindle orientation and asymmetric cytokinesis in the mouse small intes-
1162 tine. *J. Histochem. Cytochem.* 55, 1173–1180.
- 1163 Furuse, M., and Izumi, Y. (2017). Molecular dissection of smooth septate junctions: understanding
1164 their roles in arthropod physiology. *Ann N Y Acad Sci* 1397, 17–24.

- 1165 Gilbert, T., and Rodriguez-Boulan, E. (1991). Induction of vacuolar apical compartments in the Ca-
1166 co-2 intestinal epithelial cell line. *Journal of Cell Science* *100*, 451–458.
- 1167 Guillot, C., and Lecuit, T. (2013). Mechanics of epithelial tissue homeostasis and morphogenesis.
1168 *Science* *340*, 1185–1189.
- 1169 He, L., Binari, R., Huang, J., Falo-Sanjuan, J., and Perrimon, N. (2019). In vivo study of gene expres-
1170 sion with an enhanced dual-color fluorescent transcriptional timer. *ELife* *8*, e46181.
- 1171 Izumi, Y., Motoishi, M., Furuse, K., and Furuse, M. (2016). A tetraspanin regulates septate junction
1172 formation in *Drosophila* midgut. *J Cell Sci* *129*, 1155–1164.
- 1173 Jiang, H., and Edgar, B.A. (2009). EGFR signaling regulates the proliferation of *Drosophila* adult
1174 midgut progenitors. *Development* *136*, 483–493.
- 1175 Jin, Y., Patel, P.H., Kohlmaier, A., Pavlovic, B., Zhang, C., and Edgar, B.A. (2017). Intestinal stem
1176 cell pool regulation in *Drosophila*. *Stem Cell Reports* *8*, 1479–1487.
- 1177 Jin, Z., Chen, J., Huang, H., Wang, J., Lv, J., Yu, M., Guo, X., Zhang, Y., Cai, T., and Xi, R. (2020).
1178 The *Drosophila* Ortholog of Mammalian Transcription Factor Sox9 Regulates Intestinal Homeostasis
1179 and Regeneration at an Appropriate Level. *Cell Reports* *31*.
- 1180 Jinguji, Y., and Ishikawa, H. (1992). Electron Microscopic Observations on the Maintenance of the
1181 Tight Junction during Cell Division in the Epithelium of the Mouse Small Intestine. *Cell Struct Funct*
1182 *17*, 27–37.
- 1183 Kapuria, S., Karpac, J., Biteau, B., Hwangbo, D., and Jasper, H. (2012). Notch-Mediated Suppression
1184 of TSC2 Expression Regulates Cell Differentiation in the *Drosophila* Intestinal Stem Cell Lineage.
1185 *PLoS Genetics* *8*, e1003045.
- 1186 Kizilyaprak, C., Longo, G., Daraspe, J., and Humbel, B.M. (2015). Investigation of resins suitable for
1187 the preparation of biological sample for 3-D electron microscopy. *Journal of Structural Biology* *189*,
1188 135–146.
- 1189 Kolotuev, I. (2014). Positional Correlative Anatomy of Invertebrate Model Organisms Increases Effi-
1190 ciency of TEM Data Production. *Microscopy and Microanalysis* *20*, 1392–1403.
- 1191 Kolotuev, I., and Micheva, K.D. (2019). Can Correlative Microscopy Ever Be Easy? An Array To-
1192 mography Viewpoint. In *Correlative Imaging*, (John Wiley & Sons, Ltd), pp. 81–98.
- 1193 Kolotuev, I., Schwab, Y., and Labouesse, M. (2010). A precise and rapid mapping protocol for cor-
1194 relative light and electron microscopy of small invertebrate organisms. *Biology of the Cell* *102*, 121–
1195 132.
- 1196 Korzelius, J., Naumann, S.K., Loza-Coll, M.A., Chan, J.S., Dutta, D., Oberheim, J., Gläßer, C.,
1197 Southall, T.D., Brand, A.H., Jones, D.L., et al. (2014). Escargot maintains stemness and suppresses
1198 differentiation in *Drosophila* intestinal stem cells. *EMBO J* *33*, 2967–2982.
- 1199 Koyama, L.A.J., Aranda-Díaz, A., Su, Y.-H., Balachandra, S., Martin, J.L., Ludington, W.B., Huang,
1200 K.C., and O’Brien, L.E. (2020). Bellymount enables longitudinal, intravital imaging of abdominal
1201 organs and the gut microbiota in adult *Drosophila*. *PLOS Biology* *18*, e3000567.

- 1202 Kremer, J.R., Mastronarde, D.N., and McIntosh, J.R. (1996). Computer Visualization of Three-
1203 Dimensional Image Data Using IMOD. *Journal of Structural Biology* 116, 71–76.
- 1204 Lattner, J., Leng, W., Knust, E., Brankatschk, M., and Flores-Benitez, D. (2019). Crumbs organizes
1205 the transport machinery by regulating apical levels of PI(4,5)P2 in *Drosophila*. *ELife* 8, e50900.
- 1206 Leblond, C.P. (1981). The life history of cells in renewing systems. *Am. J. Anat.* 160, 114–158.
- 1207 Lee, T., and Luo, L. (1999). Mosaic analysis with a repressible cell marker for studies of gene func-
1208 tion in neuronal morphogenesis. *Neuron* 22, 451–461.
- 1209 Lee, W.-C., Beebe, K., Sudmeier, L., and Micchelli, C.A. (2009). Adenomatous polyposis coli regu-
1210 lates *Drosophila* intestinal stem cell proliferation. *Development* 136, 2255–2264.
- 1211 Lemaitre, B., and Miguel-Aliaga, I. (2013). The Digestive Tract of *Drosophila melanogaster*. *Annu*
1212 *Rev Genet* 47, 377–404.
- 1213 Leung, C.T., Coulombe, P.A., and Reed, R.R. (2007). Contribution of olfactory neural stem cells to
1214 tissue maintenance and regeneration. *Nat Neurosci* 10, 720–726.
- 1215 Liang, J., Balachandra, S., Ngo, S., and O’Brien, L.E. (2017). Feedback regulation of steady-state
1216 epithelial turnover and organ size. *Nature* 548, 588–591.
- 1217 Linden, S.K., Sutton, P., Karlsson, N.G., Korolik, V., and McGuckin, M.A. (2008). Mucins in the
1218 mucosal barrier to infection. *Mucosal Immunology* 1, 183–197.
- 1219 Lowery, L.A., Rienzo, G.D., Gutzman, J.H., and Sive, H. (2009). Characterization and Classification
1220 of Zebrafish Brain Morphology Mutants. *The Anatomical Record* 292, 94–106.
- 1221 Macara, I.G., Guyer, R., Richardson, G., Huo, Y., and Ahmed, S.M. (2014). Epithelial Homeostasis.
1222 *Current Biology* 24, R815–R825.
- 1223 Madara, J.L. (1987). Intestinal absorptive cell tight junctions are linked to cytoskeleton. *American*
1224 *Journal of Physiology-Cell Physiology* 253, C171–C175.
- 1225 Marianes, A., and Spradling, A.C. (2013). Physiological and stem cell compartmentalization within
1226 the *Drosophila* midgut. *ELife* 2, 155.
- 1227 Martin, J.L., Sanders, E.N., Moreno-Roman, P., Jaramillo Koyama, L.A., Balachandra, S., Du, X.,
1228 and O’Brien, L.E. (2018). Long-term live imaging of the *Drosophila* adult midgut reveals real-time
1229 dynamics of division, differentiation and loss. *ELife* 7, e36248.
- 1230 McGuckin, M.A., Lindén, S.K., Sutton, P., and Florin, T.H. (2011). Mucin dynamics and enteric
1231 pathogens. *Nature Reviews Microbiology* 9, 265–278.
- 1232 McGuire, S.E., Le, P.T., Osborn, A.J., Matsumoto, K., and Davis, R.L. (2003). Spatiotemporal rescue
1233 of memory dysfunction in *Drosophila*. *Science* 302, 1765–1768.
- 1234 McKinley, K.L., Stuurman, N., Royer, L.A., Schartner, C., Castillo-Azofeifa, D., Delling, M., Klein,
1235 O.D., and Vale, R.D. (2018). Cellular aspect ratio and cell division mechanics underlie the patterning
1236 of cell progeny in diverse mammalian epithelia. *ELife* 7, e36739.

- 1237 McMahon, A., Supatto, W., Fraser, S.E., and Stathopoulos, A. (2008). Dynamic Analyses of Drosophila Gastrulation Provide Insights into Collective Cell Migration. *Science* 322, 1546–1550.
1238
- 1239 Meng, F.W., Rojas Villa, S.E., and Biteau, B. (2020). Sox100B Regulates Progenitor-Specific Gene Expression and Cell Differentiation in the Adult Drosophila Intestine. *Stem Cell Reports* 14, 226–240.
1240
- 1241 Merzdorf, C.S., Chen, Y.-H., and Goodenough, D.A. (1998). Formation of Functional Tight Junctions in Xenopus Embryos. *Developmental Biology* 195, 187–203.
1242
- 1243 Micchelli, C.A., and Perrimon, N. (2006). Evidence that stem cells reside in the adult Drosophila midgut epithelium. *Nature* 439, 475–479.
1244
- 1245 Michael J. Evans, C.G.P., Laura S. Van Winkle, Michelle V. Fanucchi (2001). Cellular and Molecular Characteristics of Basal Cells in Airway Epithelium. *Experimental Lung Research* 27, 401–415.
1246
- 1247 de Navascués, J., Perdigoto, C.N., Bian, Y., Schneider, M.H., Bardin, A.J., Martínez-Arias, A., and Simons, B.D. (2012). Drosophila midgut homeostasis involves neutral competition between symmetrically dividing intestinal stem cells. *EMBO J* 31, 2473–2485.
1248
1249
- 1250 Nie, Y., Li, Q., Amcheslavsky, A., Duhart, J.C., Veraksa, A., Stocker, H., Raftery, L.A., and Ip, Y.T. (2015). Bunched and Madm Function Downstream of Tuberous Sclerosis Complex to Regulate the Growth of Intestinal Stem Cells in Drosophila. *Stem Cell Rev and Rep* 11, 813–825.
1251
1252
- 1253 O’Brien, L.E. (2013). Regional specificity in the Drosophila midgut: setting boundaries with stem cells. *Cell Stem Cell* 13, 375–376.
1254
- 1255 O’Brien, L.E., Zegers, M.M.P., and Mostov, K.E. (2002). Opinion: Building epithelial architecture: insights from three-dimensional culture models. *Nat Rev Mol Cell Biol* 3, 531–537.
1256
- 1257 O’Brien, L.E., Soliman, S.S., Li, X., and Bilder, D. (2011). Altered modes of stem cell division drive adaptive intestinal growth. *Cell* 147, 603–614.
1258
- 1259 Ohlstein, B., and Spradling, A. (2006). The adult Drosophila posterior midgut is maintained by pluripotent stem cells. *Nature* 439, 470–474.
1260
- 1261 Ohlstein, B., and Spradling, A. (2007). Multipotent Drosophila intestinal stem cells specify daughter cell fates by differential Notch signaling. *Science* 315, 988–992.
1262
- 1263 Overeem, A.W., Bryant, D.M., and van IJzendoorn, S.C.D. (2015). Mechanisms of apical–basal axis orientation and epithelial lumen positioning. *Trends in Cell Biology* 25, 476–485.
1264
- 1265 Parslow, A., Cardona, A., and Bryson-Richardson, R.J. (2014). Sample drift correction following 4D confocal time-lapse imaging. *J Vis Exp* e51086–e51086.
1266
- 1267 Pellettieri, J., and Alvarado, A.S. (2007). Cell turnover and adult tissue homeostasis: From humans to planarians. *Annu Rev Genet* 41, 83–105.
1268
- 1269 Perdigoto, C.N., Schweisguth, F., and Bardin, A.J. (2011). Distinct levels of Notch activity for commitment and terminal differentiation of stem cells in the adult fly intestine. *Development* 138, 4585–4595.
1270
1271

- 1272 Quan, Z., Sun, P., Lin, G., and Xi, R. (2013). TSC1/2 regulates intestinal stem cell maintenance and
1273 lineage differentiation through Rheb–TORC1–S6K but independently of nutritional status or Notch
1274 regulation. *J Cell Sci* *126*, 3884–3892.
- 1275 Rock, J.R., Onaitis, M.W., Rawlins, E.L., Lu, Y., Clark, C.P., Xue, Y., Randell, S.H., and Hogan,
1276 B.L.M. (2009). Basal cells as stem cells of the mouse trachea and human airway epithelium. *Proceed-*
1277 *ings of the National Academy of Sciences* *106*, 12771–12775.
- 1278 Ruiz-Herrero, T., Alessandri, K., Gurchenkov, B.V., Nassoy, P., and Mahadevan, L. (2017). Organ
1279 size control via hydraulically gated oscillations. *Development* *144*, 4422–4427.
- 1280 Schindelin, J., Arganda-Carreras, I., Frise, E., Kaynig, V., Longair, M., Pietzsch, T., Preibisch, S.,
1281 Rueden, C., Saalfeld, S., Schmid, B., et al. (2012). Fiji: an open-source platform for biological-image
1282 analysis. *Nat Methods* *9*, 676–682.
- 1283 Sedzinski, J., Hannezo, E., Tu, F., Biro, M., and Wallingford, J.B. (2016). Emergence of an Apical
1284 Epithelial Cell Surface In Vivo. *Developmental Cell* *36*, 24–35.
- 1285 Sedzinski, J., Hannezo, E., Tu, F., Biro, M., and Wallingford, J.B. (2017). RhoA regulates actin net-
1286 work dynamics during apical surface emergence in multiciliated epithelial cells. *J Cell Sci* *130*, 420–
1287 428.
- 1288 Sekiya, K., Futaesaku, Y., and Nakase, Y. (1988). Electron microscopic observations on tracheal epi-
1289 thelia of mice infected with *Bordetella bronchiseptica*. *Microbiol. Immunol.* *32*, 461–472.
- 1290 Sigurbjörnsdóttir, S., Mathew, R., and Leptin, M. (2014). Molecular mechanisms of de novo lumen
1291 formation. *Nat Rev Mol Cell Biol* *15*, 665–676.
- 1292 Stubbs, J.L., Davidson, L., Keller, R., and Kintner, C. (2006). Radial intercalation of ciliated cells
1293 during *Xenopus* skin development. *Development* *133*, 2507–2515.
- 1294 Taniguchi, K., Shao, Y., Townshend, R.F., Cortez, C.L., Harris, C.E., Meshinchi, S., Kalantry, S., Fu,
1295 J., O’Shea, K.S., and Gumucio, D.L. (2017). An apicosome initiates self-organizing morphogenesis
1296 of human pluripotent stem cells. *J Cell Biol* *216*, 3981–3990.
- 1297 Tsujimura, A., Koikawa, Y., Salm, S., Takao, T., Coetzee, S., Moscatelli, D., Shapiro, E., Lepor, H.,
1298 Sun, T.-T., and Wilson, E.L. (2002). Proximal location of mouse prostate epithelial stem cells : a
1299 model of prostatic homeostasis. *Journal of Cell Biology* *157*, 1257–1265.
- 1300 Varadarajan, S., Stephenson, R.E., and Miller, A.L. (2019). Multiscale dynamics of tight junction
1301 remodeling. *J Cell Sci* *132*.
- 1302 Vasquez, C.G., Vachharajani, V.T., Garzon-Coral, C., and Dunn, A.R. (2021). Physical basis for the
1303 determination of lumen shape in a simple epithelium. *Nature Communications*.
- 1304 Vega-Salas, D.E. (1988). Exocytosis of vacuolar apical compartment (VAC): a cell-cell contact con-
1305 trolled mechanism for the establishment of the apical plasma membrane domain in epithelial cells.
1306 *The Journal of Cell Biology* *107*, 1717–1728.
- 1307 Viitanen, A., Gullmets, J., Morikka, J., Katajisto, P., Mattila, J., and Hietakangas, V. (2021). An im-
1308 age analysis method for regionally defined cellular phenotyping of the *Drosophila* midgut. *Cell Re-*
1309 *ports Methods* 100059.

- 1310 Voiculescu, O., Bertocchini, F., Wolpert, L., Keller, R.E., and Stern, C.D. (2007). The amniote primi-
1311 tive streak is defined by epithelial cell intercalation before gastrulation. *Nature* *449*, 1049–1052.
- 1312 Walck-Shannon, E., and Hardin, J. (2014). Cell intercalation from top to bottom. *Nat Rev Mol Cell*
1313 *Biol* *15*, 34–48.
- 1314 Wang, A.Z., Ojakian, G.K., and Nelson, W.J. (1990). Steps in the morphogenesis of a polarized epi-
1315 thelium. I. Uncoupling the roles of cell-cell and cell-substratum contact in establishing plasma mem-
1316 brane polarity in multicellular epithelial (MDCK) cysts. *Journal of Cell Science* *95* (Pt 1), 137–151.
- 1317 Xiang, J., Bandura, J., Zhang, P., Jin, Y., Reuter, H., and Edgar, B.A. (2017). EGFR-dependent TOR-
1318 independent endocycles support *Drosophila* gut epithelial regeneration. *Nat Commun* *8*, 15125.
- 1319 Xu, C., Tang, H.-W., Hung, R.-J., Hu, Y., Ni, X., Housden, B.E., and Perrimon, N. (2019). The Sep-
1320 tate Junction Protein Tsp2A Restricts Intestinal Stem Cell Activity via Endocytic Regulation of aPKC
1321 and Hippo Signaling. *Cell Rep* *26*, 670-688.e6.
- 1322 Yanagihashi, Y., Usui, T., Izumi, Y., Yonemura, S., Sumida, M., Tsukita, S., Uemura, T., and Furuse,
1323 M. (2012). A novel smooth septate junction-associated membrane protein, Snakeskin, is required for
1324 intestinal barrier function in *Drosophila*. *Journal of Cell Science* *125*, 1980–1990.
- 1325 Yang, Q., Xue, S.-L., Chan, C.J., Rempfler, M., Vischi, D., Maurer-Gutierrez, F., Hiiragi, T., Han-
1326 nez, E., and Liberali, P. (2021). Cell fate coordinates mechano-osmotic forces in intestinal crypt
1327 formation. *Nat Cell Biol* *23*, 733–744.
- 1328 Yu, H.H., and Zallen, J.A. (2020). Abl and Canoe/Afadin mediate mechanotransduction at tricellular
1329 junctions. *Science* *370*.
- 1330